

Robust Odometry and Mapping for Multi-LiDAR Systems with Online Extrinsic Calibration

Jianhao Jiao, *Student Member, IEEE*, Haoyang Ye, *Student Member, IEEE*, Yilong Zhu, *Student Member, IEEE*, and Ming Liu, *Senior Member, IEEE*

Abstract—Combining multiple LiDARs enables a robot to maximize its perceptual awareness of environments and obtain sufficient measurements, which is promising for simultaneous localization and mapping (SLAM). This paper proposes a system to achieve robust and simultaneous extrinsic calibration, odometry, and mapping for a multiple LiDARs. Our approach starts with measurement preprocessing to extract edge and planar features from raw measurements. After a motion and extrinsic initialization procedure, a sliding window-based multi-LiDAR odometry runs onboard to estimate poses with online calibration refinement and convergence identification. We further develop a mapping algorithm to construct a global map and optimize poses with sufficient features together with a method to model and reduce data uncertainty. We validate our approach’s performance with extensive experiments on ten sequences (4.60km total length) for the calibration and SLAM and compare them against the state-of-the-art. We demonstrate that the proposed work is a complete, robust, and extensible system for various multi-LiDAR setups. The source code, datasets, and demonstrations are available at: <https://ram-lab.com/file/site/m-loam>.

Index Terms—SLAM, calibration and identification, sensor fusion, autonomous vehicle navigation

I. INTRODUCTION

A. Motivation

SIMULTANEOUS Localization and Mapping (SLAM) is essential to a wide range of applications, such as scene reconstruction, robotic exploration, and autonomous driving [1]–[3]. Approaches that use only a LiDAR have attracted much attention from the research community due to their accuracy and reliability in range measurements. However, LiDAR-based methods commonly suffer from data sparsity and limited vertical field of view (FOV) in real-world applications [4]. For instance, LiDARs’ points distribute loosely, which induces a mass of empty regions between two nearby scans. This characteristic usually causes state estimation to degenerate in structureless environments, such as narrow corridors and stairs [5]. Recently, owing to the decreasing price of sensors, we have seen a growing trend of deploying multi-LiDAR systems on practical robotic platforms [6]–[11]. Compared with a single-LiDAR setup, the primary improvement of multi-LiDAR systems is that the sensing range and density of measurements are enhanced significantly. This impact is practically useful for self-driving cars since we have to address the critical blind spots created by the vehicle body. Thus, we consider multi-LiDAR systems in this paper.

Jianhao Jiao, Haoyang Ye, Yilong Zhu, and Ming Liu are with the Department of Electrical and Computer Engineering, Hong Kong University of Science and Technology, Kowloon, Hong Kong, China (email: {jjiao, hyeab, yzhubr, eelium}@ust.hk).

B. Challenges

Despite its great advantages for environmental perception, a number of issues affect the development of SLAM using a multi-LiDAR setup.

1) *Precise and Flexible Extrinsic Calibration*: Recovering the multi-LiDAR transformations from a new robotic configuration is complicated. In many cases, professional users have to calibrate these sensors in human-made surroundings [12] carefully. This requirement increases the cost to deploy and maintain a multi-LiDAR system for field robots.

It is desirable that the system can *self-calibrate* the extrinsics in various environments online. As shown in [13]–[15], benefiting from the simultaneous estimation of extrinsics and ego-motion, the working scope of visual-inertial systems has been expanded to drones and vessels in outdoor scenes. These approaches continuously perform calibration during the mission to guarantee that objective function is always ‘optimal.’ But this process typically requires environmental or motion constraints with full observability. Otherwise, the resulting extrinsics may become suboptimal or unreliable. Thus, we have to fix the extrinsics if they are accurate, which creates a demand for online calibration with convergence identification. In order to cope with the centimeter-level calibration error and unexpected changes on extrinsics over time, it is also beneficial to model the extrinsic perturbation for multi-LiDAR systems.

2) *Low Pose Drift*: To provide accurate poses in real time, state-of-the-art (SOTA) LiDAR-based methods [16]–[18] solve SLAM by two algorithms: *odometry* and *mapping*. Generally, these algorithms are designed to estimate poses in a coarse-to-fine fashion. In the odometry algorithm, an approach that fully exploits multi-LiDAR measurements within a local window is required. The increasing constraints help to prevent degeneracy or failure in the original frame-to-frame registration. The subsequent mapping algorithm runs at a relatively low frequency and is given plenty of feature points and many iterations for better estimation results. However, as we identify in Section VIII, these SOTA approaches neglect the fact that uncertain points in the global map limit the accuracy. To minimize this adverse effect, we must develop a method to capture map points’ uncertainties and reject outliers.

C. Contributions

To tackle these challenges, we propose M-LOAM, a robust system for multi-LiDAR extrinsic calibration, real-time odometry, and mapping. Without manual intervention, our system can start with several extrinsic-uncalibrated LiDARs,

automatically calibrate their extrinsics, and provide accurate poses as well as a globally consistent map. In our previous work [5], we proposed sliding window-based odometry to fuse LiDAR points with high-frequency IMU measurements. This framework is extended in this paper, where we try to solve the problem of multi-LiDAR fusion. In addition, we introduce a motion-based approach [4] to initialize extrinsics, and employ the tools proposed in [19] to represent uncertainties of poses. Our design of M-LOAM presents *contributions* as follows:

- 1) Automatic initialization that computes all critical states, including motion between consecutive frames as well as extrinsics for subsequent phases. It can start at arbitrary positions without any prior knowledge of the mechanical configuration or calibration objects (Section VI).
- 2) Online self-calibration with a general convergence criterion is executed simultaneously with the odometry. It has the capability to monitor the convergence and trigger termination in a fully unsupervised manner (Section VII-B).
- 3) Sliding window-based odometry that can jointly exploit information from multiple LiDARs. This implementation is explained as small-scale frame-to-map registration, which further reduces the drift accumulated by the consecutive frame-to-frame odometry (Section VII-C).
- 4) Mapping with a two-stage approach that captures and propagates points' uncertainties from sensor noise, degenerate pose estimation, and extrinsic perturbation. This approach enables the mapping process with an awareness of uncertainty and helps us to maintain the consistency of a global map as well as boost the robustness of a system for long-duration navigation tasks (Section VIII).

To the best of our knowledge, M-LOAM is the first complete solution to multi-LiDAR calibration and SLAM. The whole system is evaluated under extensive experiments on both handheld devices and autonomous vehicles, covering various scenarios from indoor offices to outdoor urban roads, and outperforms the SOTA LiDAR-based methods. Regarding the calibration on these platforms, our approach achieves an extrinsic accuracy of centimeters in translation and deci-degrees in rotation. For the SLAM in different scales, M-LOAM has been successfully applied to provide accurate poses and map results. To benefit the research community, we publicly release our code, implementation details, and multi-LiDAR datasets.

D. Organization

The rest of the paper is organized as follows. Section II reviews the relevant literature. Section III formulates the problem as a Maximum Likelihood Estimation (MLE). Section IV gives the nomenclature and an overview of the system. Section V describes the measurement preprocessing module on LiDARs. Section VI introduces the motion and extrinsic initialization procedure. Section VII presents the tightly coupled, optimization-based M-LO with online calibration refinement. The uncertainty-aware multi-LiDAR mapping algorithm is introduced in Section VIII, followed by the experimental results in Section IX. In Section X, we provide a discussion about the proposed system. Finally, Section XI concludes this paper with possible future research directions.

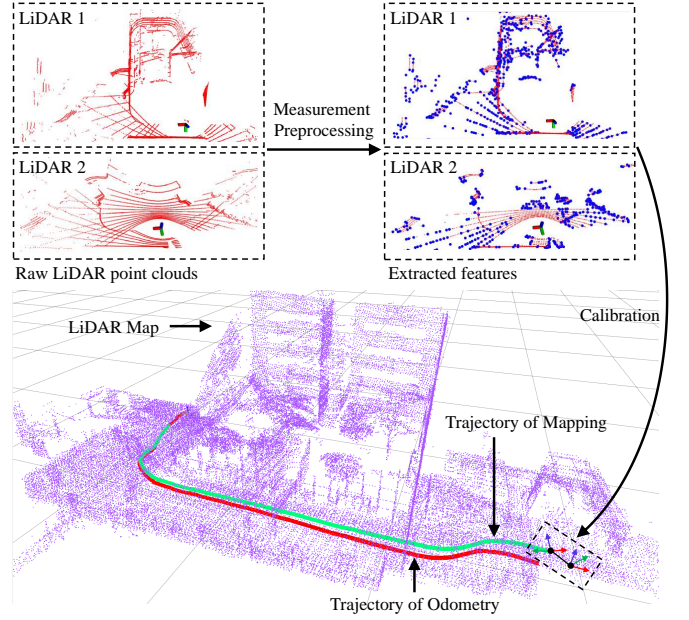


Fig. 1. We visualize the immediate results of M-LOAM. The raw point clouds perceived by different LiDAR are denoised and extracted with edge and planar features, which are shown as blue dots (edge points) and red dots (planar points) at the top-right position. Online calibration is performed to obtain accurate extrinsics. After that, the odometry and mapping algorithms use the features to estimate poses sequentially. The trajectory of mapping (green) is more accurate than that of odometry (red).

II. RELATED WORK

Scholarly works on SLAM and extrinsic calibration are extensive. In this section, we briefly review relevant results on LiDAR-based SLAM and online calibration methods for multi-sensor systems.

A. LiDAR-Based SLAM

Generally, many SOTA are developed from the iterative closest point (ICP) algorithm [20]–[23], into which the methods including measurement preprocessing, degeneracy prediction, and sensor fusion are incorporated. These works have pushed the current LiDAR-based systems to become fast, robust, and feasible to large-scale environments.

1) *Measurement Preprocessing*: As the front-end of a system, the measurement preprocessing encodes point clouds into a compact representation. We categorize related algorithms into either dense or sparse methods. As a typical dense method, SuMa [24] demonstrated the advantages of utilizing surfel-based maps for registration and loop detection. Its extended version [25] was proposed to incorporate semantic constraints into the original cost function. However, the process of matching dense pixel-to-pixel correspondences in these methods is time-consuming. These approaches are not applicable to our cases since we have to frequently perform the registration.

Sparse methods prefer to extract geometric features from raw measurements and are thus supposed to have real-time performance. Grant et al. [26] proposed a plane-based registration, while Velas et al. [27] represented point clouds as collar line segments. Compared to them, LOAM [16] has fewer assumptions about sensors and surroundings. It selects distinct

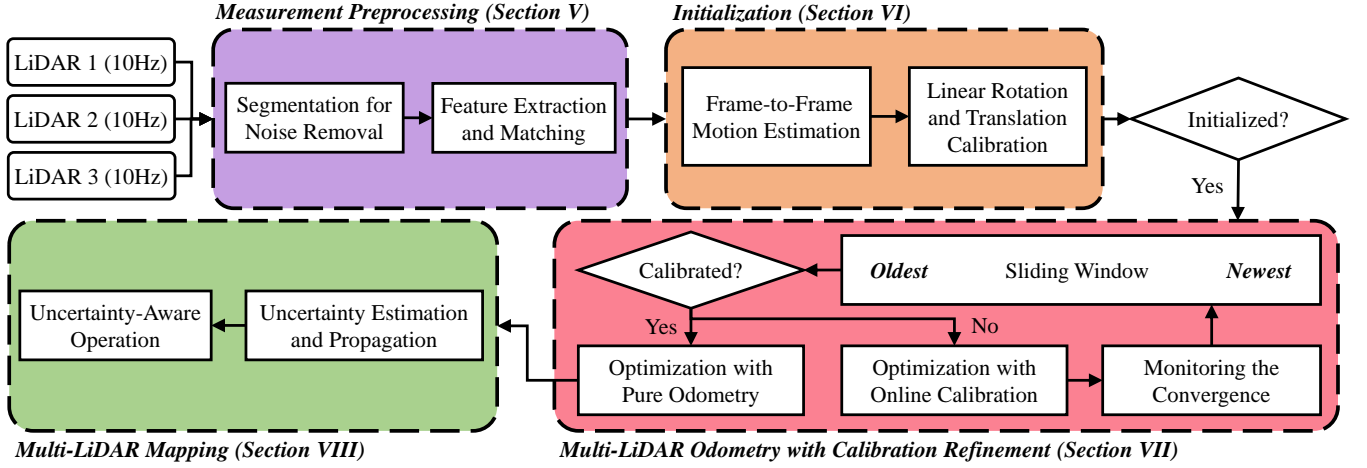


Fig. 2. The block diagram illustrating the full pipeline of the proposed M-LOAM system. The system starts with measurement preprocessing (Section V). The initialization module (Section VI) initializes values for the subsequent nonlinear optimization-based multi-LiDAR odometry with calibration refinement (Section VII). According to the convergence of calibration, the optimization is divided into two subtasks: online calibration and pure odometry. Finally, the uncertainty-aware multi-LiDAR mapping (Section VIII) maintains a globally consistent map to decrease pose drift and noisy points.

points from both edge lines and local planar patches. Later, several following methods employed ground planes [28], clustering techniques [17], visual detection [29], probabilistic grid maps [30], or directly used dense scanners [18], [31], [32] to improve the performance of sparse approaches in noisy or structure-less environments. To limit the computation time when more LiDARs are involved, we extract the sparse edge and planar features like LOAM. But differently, we represent their residuals in a more concise and unified way.

2) *Degeneracy in State Estimation*: The geometric constraints of features are formulated as an ego-motion optimization problem. Different methods have been proposed to tackle the degeneracy issue. Zhang et al. [33] defined a *factor*, which is equal to the minimum eigenvalue of information matrices to determine the degeneracy. They also proposed a technique called solution remapping to update states in well-conditioned directions. As demonstrated in [34]–[36], this technique has been applied to tasks including localization, registration, pose graph optimization, and sensor fusion. To quantify the observability of a nonlinear system, Rong et al. [37] used the eigenvalues of the Empirical Observability Gramian. Since our problem is similar to that of Zhang et al. [33], we introduce their method to update variables only in well-constrained directions. Additionally, our online calibration method employs the *degeneracy factor* as a metric to measure the quality of the extrinsic estimation.

3) *Sensor Fusion*: Integrating a LiDAR system with visual or inertial measurements dramatically improves the motion-tracking performance under rapid motion. The simplest way to deal with multi-modal measurements is the loosely coupled fusion, where the pose estimation of each sensor is treated independently. Taking the LiDAR-IMU setup as an example, the fusion is usually done by the extended Kalman filter (EKF) [38]–[40]. In the EKF framework, the IMU propagates states and corrects skewed points. The prior states are further optimized by the LiDAR-based odometry and mapping. Tightly coupled algorithms that jointly optimize all measurements

and poses of sensors have become increasingly prevalent in the community. They are usually implemented by either the EKF [41]–[43] or sliding window estimator [5], [44]–[46]. In addition, there are methods performing LiDAR-camera-IMU fusion in a coarse manner, e.g., using depth map generation [47], visual features [48], sequential prediction [35], and visual localization in a prior LiDAR map [49]–[51]. In contrast to these setups, the primary advantage of adapting a multi-LiDAR system is to maximize the sensing coverage against extreme occlusion. Stimulated by these works in [5], [15], we implement a tightly coupled method within a bounded-size sliding window to estimate states of multiple LiDARs.

B. Multi-Sensor Calibration

Precise extrinsic calibration is of paramount importance to any multi-sensor system. Traditional methods [12], [52]–[54] have to run an ad-hoc calibration procedure before a mission. This tedious process needs to be repeated whenever there is any perturbation on the robot configuration. A more flexible solution to estimate these parameters is to combine with SLAM-based techniques. Here, the extrinsics are treated as state variables and thus optimized along with the poses of sensors. This scheme is also applicable to some non-stationary parameters, such as the robot kinematics and IMU biases.

Kummerle et al. [55] pioneered a hyper-graph optimization framework to calibrate an onboard laser scanner with wheel encoders. Their experiments reveal that online parameter correction can lead to consistent and accurate results. Teichman et al. [56] proposed an iterative SLAM-fitting pipeline to resolve the distortion of two RGB-D cameras. To recover the spatial offsets of a multi-camera system, Heng et al. [57] formulated the problem as a bundle adjustment, while Ouyang et al. [58] employed the Ackermann steering model of vehicles to constrain the extrinsics. As presented in [5], [59]–[61], robust initialization and online estimation for IMU biases and extrinsics are also crucial to the visual- or LiDAR-inertial systems. Similarly, our approach follows the online procedure to

achieve flexible multi-LiDAR extrinsic calibration. To monitor the convergence of estimated extrinsics, we further propose a general criterion. Another improvement is that our system models the extrinsic perturbation to reduce its negative effect on long-term navigation tasks.

III. PROBLEM STATEMENT

We first discuss the MLE, which serves as the basis of M-LOAM. We then show that how MLE is implemented for extrinsics and pose estimation in multi-LiDAR systems.

A. Maximum Likelihood Estimation

We formulate the problem of state estimation as a MLE given a set of observations [62]. At the k^{th} frame, the state is denoted by \mathbf{x}_k . The set of observations $\mathcal{F}_k = [\mathbf{p}_{k1}, \dots, \mathbf{p}_{km}]$ gathers m available measurements. The MLE computes the most likely state that maximizes the pdf as:

$$\hat{\mathbf{x}}_k = \arg \max_{\mathbf{x}_k} p(\mathcal{F}_k | \mathbf{x}_k) = \arg \max_{\mathbf{x}_k} \prod_{i=1}^m p(\mathbf{p}_{ki} | \mathbf{x}_k). \quad (1)$$

The measurement model $\mathbf{h}(\mathbf{x})$ is subjected to a Gaussian noise: $\mathbf{p}_{ki} = \mathbf{h}_i(\mathbf{x}_k) + \mathbf{n}_i$, where $\mathbf{n}_i \sim \mathcal{N}(\mathbf{0}, \Sigma_i)$. Maximizing the pdf is equivalent to solve a least-squares problem:

$$\hat{\mathbf{x}}_k = \arg \min_{\mathbf{x}_k} \frac{1}{2} \sum_{i=1}^m \|\mathbf{h}_i(\mathbf{x}_k) - \mathbf{p}_{ki}\|_{\Sigma_i}^2, \quad (2)$$

where $\|\mathbf{a}\|_{\Sigma}^2 = \mathbf{a}^T \Sigma^{-1} \mathbf{a}$. Iterative methods such as Gauss-Newton or Levenberg-Marquardt are often used to address (2). We first perform the first-order linear approximation of the nonlinear residual function $\mathbf{r}_i(\mathbf{x}_k) \triangleq \mathbf{h}_i(\mathbf{x}_k) - \mathbf{p}_{ki}$ as:

$$\|\mathbf{r}_i(\mathbf{x}_k)\| \approx \|\mathbf{r}_i(\tilde{\mathbf{x}}_k^{(\ell)}) + \mathbf{J}_i(\tilde{\mathbf{x}}_k^{(\ell)})\delta\mathbf{x}\|^2, \quad (3)$$

where \mathbf{J}_i is the Jacobian of $\mathbf{r}_i(\cdot)$ linearized about the initial guess $\tilde{\mathbf{x}}_k^{(\ell)}$ at the ℓ^{th} iteration and $\delta\mathbf{x}$ is the update step. Substituting (2) with (3), the least-squares formula yields:

$$\delta\hat{\mathbf{x}} = \arg \min_{\delta\mathbf{x}} \frac{1}{2} \|\mathbf{A}\delta\mathbf{x} + \mathbf{b}\|^2, \quad (4)$$

where the matrix \mathbf{A} and the vector \mathbf{b} are defined as $\mathbf{A} \triangleq \sum_{i=1}^m \Sigma_i^{-1/2} \mathbf{J}_i$, and $\mathbf{b} \triangleq \sum_{i=1}^m \Sigma_i^{-1/2} \mathbf{r}_i$, respectively. The closed-form solution is obtained according to:

$$\delta\hat{\mathbf{x}} = -(\mathbf{A}^T \mathbf{A})^{-1} \mathbf{A}^T \mathbf{b}, \quad \text{or} \quad \delta\hat{\mathbf{x}} = -\Lambda^{-1} \mathbf{g}, \quad (5)$$

where Λ is the *information matrix* and \mathbf{g} is the *information vector* [3]. The current state is updated via $\hat{\mathbf{x}}_k^{(\ell+1)} = \tilde{\mathbf{x}}_k^{(\ell)} + \delta\hat{\mathbf{x}}$. The least-squares covariance of the state is calculated as:

$$\begin{aligned} \Xi &= E[(\mathbf{x}_k - \hat{\mathbf{x}}_k)(\mathbf{x}_k - \hat{\mathbf{x}}_k)^T] \\ &= \Lambda^{-1} \left(\sum_{i=1}^m \mathbf{J}_i^T \Sigma_i^{-1} E[\mathbf{n}_i \mathbf{n}_i^T] \Sigma_i^{-1} \mathbf{J}_i \right) \Lambda^{-1} = \Lambda^{-1}. \end{aligned} \quad (6)$$

TABLE I
NOMENCLATURE

Notation	Explanation
Coordinate System and Pose Representation	
$()^w, ()^b, ()^{i^i}$	Frame of the world, base sensor, and i^{th} LiDAR
$()^{i^i_k}$	Frame of the i^{th} LiDAR while taking the k^{th} point cloud
I	Total number of LiDARs in a multi-LiDAR system
\mathbf{p}	3-D Point
\mathbf{x}	State vector
\mathbf{t}	Translation vector in \mathbb{R}^3
\mathbf{q}	Quaternion
\mathbf{R}	Rotation matrix in the <i>Lie group</i> $SO(3)$
\mathbf{T}	Transformation matrix in the <i>Lie group</i> $SE(3)$
Odometry and Mapping	
\mathcal{F}	Features which are extracted from raw point clouds
\mathcal{E}, \mathcal{H}	Edge and planar subset of extracted features
L, Π	Edge line and planar patch
$[\mathbf{w}, d]$	Coefficient vector of a planar patch
\mathcal{M}	Local map
\mathcal{G}	Global map
λ	Degeneracy factor
ξ, ζ, θ	Gaussian noise variable
Σ	Covariance matrix of residuals
\mathbf{Z}	Covariance matrix of LiDAR depth measurement noise
Ξ	Covariance matrix of pose noise

B. Implementation in M-LOAM

We extend the MLE to propose multiple estimators in M-LOAM to solve the robot poses and extrinsics in a coarse-to-fine fashion in these equations: (9), (20), and (23). Three modifications have been made:

- In odometry, we consider that the Gaussian noise stems from LiDARs' depth measurement errors (also called sensor noise) due to factors such as target distance [63]. We set $\Sigma = \mathbf{Z}$ as a constant matrix¹. In mapping, Σ is propagated according to derivations in Section VIII.
- We substitute the quadratic cost with a robust Huber loss $\rho(\cdot)$ [64] in all estimators to handle outliers.
- We propose a fixed-lag estimator to optimize all states within a sliding window in (20). The problem is formulated as a Maximum-A-Posteriori (MAP) by considering the prior information from marginalized states [65].

IV. SYSTEM OVERVIEW

The nomenclature is shown in Table I. Our system consists of one primary LiDAR and multiple auxiliary LiDARs. The primary LiDAR defines the base frame and thus we use $()^{i^1}$ or $()^b$ to indicate. The frames of auxiliary LiDARs are denoted by $()^{i^{i>1}}$. The x -, y -, and z - axes of a coordinate frame are pointing forward, left, and upward, respectively.

We define $\mathbf{x} = [\mathbf{t}, \mathbf{q}]$ as the state vector to denote translation and rotation. \mathbf{t} is a 3×1 vector and \mathbf{q} is the Hamilton quaternion. We primarily use quaternions to represent rotation and use rotation matrices \mathbf{R} to rotate vectors. Section VIII associates uncertainty with poses on vector space. For convenience, we represent poses using transformation matrices \mathbf{T} in this section. Besides, we denote \mathcal{F} the set of available features

¹ $\mathbf{Z} = \text{diag}(\sigma^2, \sigma^2, \sigma^2)$, where σ is the standard deviation (std) of LiDARs' depth measurements. We can refer manuals to obtain σ for a specific LiDAR.

extracted from LiDARs' raw measurements. Each feature is represented as a 3-D point: $\mathbf{p} = [x, y, z]^\top$. We make three assumptions to simplify the problem:

- LiDARs are synchronized, meaning that point clouds from multiple LiDARs are captured at the same time.
 - The platform undergoes sufficient non-degenerate motion in the period of calibration initialization.
 - The local map of the primary LiDAR should share an overlapping FOV with auxiliary LiDARs for feature matching in refinement to shorten the calibration phase.
- This can be achieved by moving the robot.

Fig. 2 presents the structure of the proposed multi-LiDAR odometry and mapping approach. The system starts with measurement preprocessing (Section V), in which edge and planar features are extracted and tracked from the denoised point clouds. The initialization module (Section VI) provides all necessary values, including poses and extrinsics, for bootstrapping the subsequent nonlinear optimization-based M-LO. The M-LO tightly fuses multi-LiDAR measurements to optimize the odometry and calibration in a sliding window. Finally, the mapping module (Section VIII) constructs a global map with sufficient features to eliminate the drift. It also performs the uncertainty-aware operation. The M-LO and mapping modules run concurrently in separated threads.

V. MEASUREMENT PREPROCESSING

We implement three sequential steps to pre-process LiDAR measurements. We first segment raw point clouds into many clusters to remove noisy objects. We then extract edge and planar features. To associate features between consecutive frames, we finally determine their correspondences. In this section, LiDARs are handled independently.

A. Segmentation for Noise Removal

With knowing the vertical scanning angles of a LiDAR, we can project the raw point cloud onto a range image without data loss. In the image, each valid point is represented by a pixel. The pixel value records the Euclidean distance from a point to the origin. We apply the segmentation method proposed in [66] to group pixels into many clusters. We assume that two neighboring points in the horizontal or vertical direction belong to one object if their connected line is roughly perpendicular ($> 60deg$) to the laser beam. The breadth-first search (BFS) algorithm is used to traverse all pixels, which assures a constant time complexity. We discard small clusters since they may provide unreliable constraints in optimization.

B. Feature Extraction and Matching

We are interested in extracting the general edge and planar features. We follow [16] to select a set of feature points from raw measurements according to their curvatures. The set of extracted features \mathcal{F} consists of two subsets: edge subset (high curve) \mathcal{E} and planar subset (low curve) \mathcal{H} . In both \mathcal{E} and \mathcal{H} , there are a portion of features which are the most representative. We further pick up edge points from \mathcal{E} with the highest curvature and planar points from \mathcal{H}

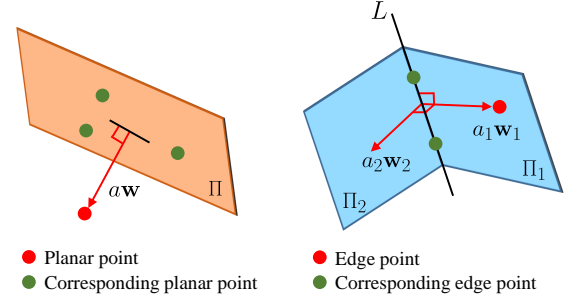


Fig. 3. The planar and edge residuals. The red dot indicates the reference point and the green dots are its corresponding points.

with the lowest curvature. These points form new sets that are denoted by $\hat{\mathcal{E}}$ and $\hat{\mathcal{H}}$, respectively. The next step is to find feature correspondences between two consecutive frames, $()^{l_{k-1}^i} \rightarrow ()^{l_k^i}$, to construct geometric constraints. For each point in $\hat{\mathcal{E}}^{l_k^i}$, two closest neighbors from $\hat{\mathcal{E}}^{l_{k-1}^i}$ are selected as edge correspondences. For a given point in $\hat{\mathcal{H}}^{l_k^i}$, three closest points from $\hat{\mathcal{H}}^{l_{k-1}^i}$ that form a plane are selected as planar correspondences.

VI. INITIALIZATION

The tightly coupled optimization of multiple LiDARs is highly nonlinear and needs accurate initial guess at the beginning. We now introduce our motion and extrinsic initialization approach. The procedure does not require any prior mechanical configuration of the sensor suite. It also does not involve any manual effort, being particularly useful for autonomous robots.

A. Scan-Based Motion Estimation

With the found correspondences between two successive frames of each LiDAR, we estimate the frame-to-frame transformation by minimizing residual errors of all features. As illustrated in Fig. 3, the residuals stem from both edge and planar correspondences. Let the state vector \mathbf{x} be the relative transformation between two scans of a LiDAR. Regarding the planar features, for a point $\mathbf{p} \in \hat{\mathcal{H}}^{l_k^i}$, if Π is the corresponding planar patch, the planar residual is computed as

$$\mathbf{r}_{\mathcal{H}}(\mathbf{x}, \mathbf{p}, \Pi) = a\mathbf{w}, \quad a = \mathbf{w}^\top (\mathbf{R}\mathbf{p} + \mathbf{t}) + d, \quad (7)$$

where a is the point-to-plane Euclidean distance and $[\mathbf{w}, d]$ is the coefficient vector of Π . Then, for an edge point $\mathbf{p} \in \hat{\mathcal{E}}^{l_k^i}$, if L is the corresponding edge line, we define the edge residual as a combination of two planar residuals using (7) as

$$\mathbf{r}_{\mathcal{E}}(\mathbf{x}, \mathbf{p}, L) = [\mathbf{r}_{\mathcal{H}}(\mathbf{x}, \mathbf{p}, \Pi_1), \mathbf{r}_{\mathcal{H}}(\mathbf{x}, \mathbf{p}, \Pi_2)], \quad (8)$$

where $[\mathbf{w}_1, d_1]$ and $[\mathbf{w}_2, d_2]$ are the coefficients of Π_1 and Π_2 , \mathbf{w}_1 coincides with the projection direction from L to \mathbf{p} , and Π_2 is perpendicular to Π_1 s.t. $\mathbf{w}_2 \perp \mathbf{w}_1$, and $\mathbf{w}_2 \perp L$. The above definitions are different from the expressions in LOAM [16], and show two benefits. Firstly, the edge residuals offer more constraints to the optimized states. Furthermore, the residuals are represented as vectors, not scalars, allowing us to multiply

a 3×3 covariance matrix. We minimize the sum of all residual errors to obtain the MLE as

$$\hat{\mathbf{x}} = \arg \min_{\mathbf{x}} \sum_{\mathbf{p} \in \hat{\mathcal{F}}_k^i} \rho \left(\|\mathbf{r}(\mathbf{x}, \mathbf{p})\|_{\Sigma_{\mathbf{p}}}^2 \right), \quad (9)$$

where the residual term is

$$\mathbf{r}(\mathbf{x}, \mathbf{p}) = \begin{cases} \mathbf{r}_{\mathcal{E}}(\mathbf{x}, \mathbf{p}, L) & \text{if } \mathbf{p} \in \hat{\mathcal{E}}_k^i \\ \mathbf{r}_{\mathcal{H}}(\mathbf{x}, \mathbf{p}, \Pi) & \text{if } \mathbf{p} \in \hat{\mathcal{H}}_k^i \end{cases}, \quad (10)$$

where the Jacobians for (9) are detailed in Appendix A.

In practice, points become skewed after a movement on LiDARs with a rolling-shutter scan. After solving the incremental motion \mathbf{x} , we can correct points' positions by transforming them into the last frame $(\cdot)^{l_{k-1}^i}$. Let t_{k-1} and t_k be the start and end time of a LiDAR scan respectively. For a point \mathbf{p} captured at $t \in (t_{k-1}, t_k]$, it is transformed as:

$$\mathbf{p}^{l_{k-1}^i} = \mathbf{R}^\tau \mathbf{p} + \tau \mathbf{t}, \quad \tau = \frac{t - t_{k-1}}{t_k - t_{k-1}}, \quad (11)$$

where²

$$\mathbf{R}^\tau = \exp(\phi^\wedge)^\tau = \exp(\tau \phi^\wedge), \quad (12)$$

where the rotation and translation are linearly interpolated.

B. Calibration of Multi-LiDAR System

The initial extrinsics are obtained by aligning the motion sequences of two sensors. This is known as solving the hand-eye calibration problem $\mathbf{A}\mathbf{X} = \mathbf{X}\mathbf{B}$, where \mathbf{A} and \mathbf{B} are the historical transformations of two sensors and \mathbf{X} is their extrinsics [67]. As the robot moves, the following equations of the i^{th} LiDAR should hold for any k

$$\mathbf{R}_{l_k^i}^{l_{k-1}^i} \mathbf{R}_{l_i}^b = \mathbf{R}_{l_i}^b \mathbf{R}_{b_k}^{b_{k-1}}, \quad (13)$$

$$(\mathbf{R}_{l_k^i}^{l_{k-1}^i} - \mathbf{I}_3) \mathbf{t}_{l_i}^b = \mathbf{R}_{l_i}^b \mathbf{t}_{b_k}^{b_{k-1}} - \mathbf{t}_{l_k^i}^{l_{k-1}^i}, \quad (14)$$

where the original problem is decomposed into the rotational and translational components.

1) *Rotation Initialization:* We rewrite (13) as a linear equation by employing the quaternion:

$$\begin{aligned} \mathbf{q}_{l_k^i}^{l_{k-1}^i} \otimes \mathbf{q}_{l_i}^b &= \mathbf{q}_{l_i}^b \otimes \mathbf{q}_{b_k}^{b_{k-1}} \\ \Rightarrow [\mathbf{Q}_1(\mathbf{q}_{l_k^i}^{l_{k-1}^i}) - \mathbf{Q}_2(\mathbf{q}_{b_k}^{b_{k-1}})] \mathbf{q}_{l_i}^b &= \mathbf{Q}_k^{k-1} \mathbf{q}_{l_i}^b \end{aligned} \quad (15)$$

where \otimes is the quaternion multiplication operator and $\mathbf{Q}_1(\cdot)$ and $\mathbf{Q}_2(\cdot)$ are the matrix representations for left and right quaternion multiplication. Stacking (15) from multiple time intervals, we form an overdetermined linear system as:

$$\begin{bmatrix} w_1^0 \cdot \mathbf{Q}_1^0 \\ \vdots \\ w_K^{K-1} \cdot \mathbf{Q}_K^{K-1} \end{bmatrix}_{4K \times 4} \mathbf{q}_{l_i}^b = \mathbf{Q}_K \mathbf{q}_{l_i}^b = \mathbf{0}_{4K \times 4}, \quad (16)$$

²The $(\cdot)^\wedge$ operator turns a 3×1 vector ϕ into a skew-symmetric matrix in the Lie algebra $\mathfrak{so}(3)$. The exponential map associates an element of $\mathfrak{so}(3)$ to a rotation matrix in $SO(3)$. Similarly, using $(\cdot)^\wedge$ and $\exp(\cdot)$ can associate an element of $\mathfrak{se}(3)$ with a transformation matrix in $SE(3)$. [19] provides detailed derivations.

where K is the number of constraints, and w_k^{k-1} are robust weights defined as the angle in the angle-axis representation of the residual quaternion:

$$\begin{aligned} w_k^{k-1} &= \rho'(\phi), \quad \phi = 2 \arctan(\|\mathbf{q}_{xyz}\|/|q_w|), \\ \mathbf{q} &= (\check{\mathbf{q}}_{l_i}^b)^* \otimes (\mathbf{q}_{l_k^i}^{l_{k-1}^i})^* \otimes \check{\mathbf{q}}_{l_i}^b \otimes \mathbf{q}_{b_k}^{b_{k-1}}, \end{aligned} \quad (17)$$

where $\rho'(\cdot)$ is the derivative of the Huber loss, $\check{\mathbf{q}}_{l_i}^b$ is the currently estimated extrinsic rotation, and \mathbf{q}^* is the inverse of \mathbf{q} . Subject to $\|\mathbf{q}_{l_i}^b\| = 1$, we find the close-form solution of (16) using SVD. For full observability of the 3-DoF rotation, sufficient motion constraints are required. Under sufficient constraints, the null space of \mathbf{Q}_K should be rank one. This means that we only have one zero singular value. Otherwise, the null space of \mathbf{Q}_K may be larger than one due to degenerate motions on one or more axes. Therefore, by checking whether this condition is achieved, we need to ensure that the second small singular value $\sigma_{\min 2}$ is large enough. We set a threshold σ_R , and terminate the rotation calibration if $\sigma_{\min 2} > \sigma_R$. The increasing data grows the height of \mathbf{Q}_K rapidly. For efficiency, we use a priority queue with a length K to incrementally maintain historical constraints. Constraints with small rotation should have priority to be removed. In experiments, the value of K should not exceed 300.

2) *Translation Initialization:* Once the rotation calibration is finished, we construct a linear system from (14) by incorporating all the available data as

$$\begin{bmatrix} \mathbf{R}_{l_1^i}^{l_0^i} - \mathbf{I}_3 \\ \vdots \\ \mathbf{R}_{l_K^i}^{l_{K-1}^i} - \mathbf{I}_3 \end{bmatrix}_{3K \times 3} \mathbf{t}_{l_i}^b = \begin{bmatrix} \hat{\mathbf{R}}_{l_i}^b \mathbf{t}_{b_1}^{b_0} - \mathbf{t}_{l_1^i}^{l_0^i} \\ \vdots \\ \hat{\mathbf{R}}_{l_i}^b \mathbf{t}_{b_K}^{b_{K-1}} - \mathbf{t}_{l_K^i}^{l_{K-1}^i} \end{bmatrix}_{3K \times 1}, \quad (18)$$

where $\mathbf{t}_{l_i}^b$ is obtained by applying the least-squares approach. However, the translation at the z -axis is unobservable if the robot motion is planar. In this case, we set $t_z = 0$ and rewrite (18) by removing the z -component of $\mathbf{t}_{l_i}^b$. Unlike [4], our method cannot initialize t_z by leveraging ground planes and must calculate it in the refinement phase (Section VII-B).

VII. TIGHTLY COUPLED MULTI-LiDAR ODOMETRY WITH CALIBRATION REFINEMENT

Taking the initial estimates as input, we propose a tightly coupled M-LO to optimize all states within a sliding window. This process is inspired by the recent success of bundle adjustment, graph-based formation, and marginalization in these multi-sensor systems [5], [15], [68].

A. Formulation

The full state vector in the sliding window is defined as

$$\begin{aligned} \mathcal{X} &= [\mathbf{x}_1, \dots, \mathbf{x}_N, \mathbf{x}_{N+1}, \mathbf{x}_{l_2}^b, \dots, \mathbf{x}_{l_I}^b], \\ \mathbf{x}_k &= [\mathbf{q}_{b_k}^w, \mathbf{t}_{b_k}^w], \quad k \in [1, N+1], \\ \mathbf{x}_{l_i}^b &= [\mathbf{q}_{l_i}^b, \mathbf{t}_{l_i}^b], \quad i \in [1, I], \end{aligned} \quad (19)$$

where \mathbf{x}_k is the state of the primary sensor in the world frame at different timestamps, $\mathbf{x}_{l_i}^b$ represents the extrinsics from the primary LiDAR to other LiDARs, and $N+1$ is the number

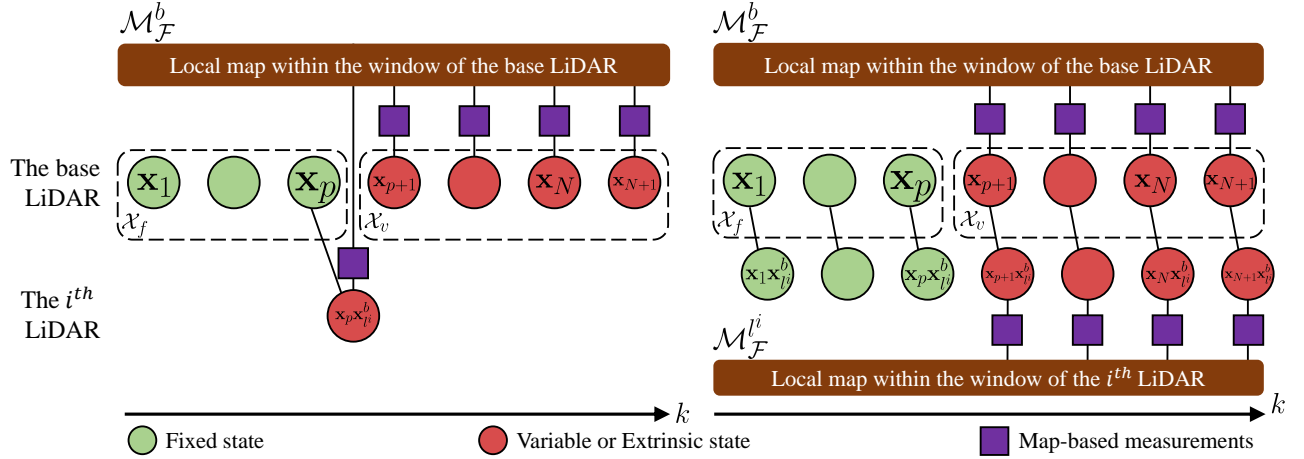


Fig. 4. Illustration of a graphical model for a sliding window estimator ($p = 3, N = 6$) with online calibration (left) and pure odometry (right). $\mathcal{M}_{\mathcal{F}}^b$ ($\mathcal{M}_{\mathcal{F}}^i$) is the local map of the base (i^{th}) LiDAR. It consists of transformed and merged feature points captured by the base (i^{th}) LiDAR from the first N frames in the window. Note that the extrinsics are optimized in the online calibration, while they are fixed in the pure odometry.

of states in the window. To estimate correspondences between these states, we build a local map. We use p to index the pivot state of the window and set \mathbf{x}_p as the origin of the local map. With the relative transformations from the pivot frame to other frames, the map is constructed by concatenating with the features at the first N frames i.e. $\mathcal{F}^{i_k}, k \in [1, N]$. The local feature map of the i^{th} LiDAR, which consists of the local edge map and local planar map, is denoted by \mathcal{M}^i . We split \mathcal{X} into three groups: \mathcal{X}_f , \mathcal{X}_v , and \mathcal{X}_e . $\mathcal{X}_f = [\mathbf{x}_1, \dots, \mathbf{x}_p]$ are considered as the fixed, accurate states. $\mathcal{X}_v = [\mathbf{x}_{p+1}, \dots, \mathbf{x}_{N+1}]$ are considered as the variable states which are updated recursively during optimization. $\mathcal{X}_e = [\mathbf{x}_{l_2}^b, \dots, \mathbf{x}_{l_t}^b]$ are the extrinsic states, whose setting, in contrast, is a little complicated. It depends on the convergence of the online calibration. We minimize the sum of all residual errors within the sliding window to obtain a MAP estimation as:

$$\hat{\mathcal{X}} = \arg \min_{\mathcal{X}} \left\{ \|\mathbf{r}_{pri}(\mathcal{X})\|^2 + f_{\mathcal{M}}(\mathcal{X}) \right\}, \quad (20)$$

where $\mathbf{r}_{pri}(\mathcal{X})$ is the prior term from state marginalization defined in Section VII-E. $f_{\mathcal{M}}(\mathcal{X})$ is the sum of residual errors from the local map. Its Jacobians (20) are given in Appendix A. Different from the recursive estimation in Section VI-A, the presented sliding window estimator jointly optimizes all states in the window. This approach outputs more accurate results since the local map provides dense and reliable correspondences. If sensors are precisely calibrated, the constraints from other LiDARs are also used. According to the convergence of calibration, we divide the problem into two subtasks: *online calibration* (variable \mathcal{X}_e) and *pure odometry* (fixed \mathcal{X}_e). At each task, the definition of $f_{\mathcal{M}}(\mathcal{X})$ is different, and we will present the details in Section VII-B and VII-C. An illustration of the sliding window estimator is shown in Fig. 4.

B. Optimization With Online Calibration

We exploit the map-based measurements to refine the coarse initialization results. Here, we treat the calibration as a registration problem. $f_{\mathcal{M}}(\mathcal{X})$ is divided into two functions w.r.t.

\mathcal{X}_v and \mathcal{X}_e . For states in \mathcal{X}_v , the constraints are constructed from correspondences between features of the primary sensor at the latest frames i.e. $\mathcal{F}^{b_k}, k \in [p+1, N+1]$ and those of the primary local map i.e. \mathcal{M}^b . For states in \mathcal{X}_e , the constraints are built up from correspondences between features of auxiliary LiDARs at the p^{th} frame i.e. \mathcal{F}^{i_p} and the map \mathcal{M}^b .

The correspondences between \mathcal{F}^{b_k} and \mathcal{M}^b are found using the method in [16]. KD-Tree is used for fast indexing in a map. For each edge point, we find a set of its nearest points in the local edge map within a specific region. This set is denoted by \mathcal{S} , and its covariance is then computed. The eigenvector associated with the largest value implies the direction of the corresponding edge line. By calculating the mean of \mathcal{S} , the position of this line is also determined. For each planar point, the coefficients of the corresponding plane in the local planar map are obtained by solving a linear system such as $\mathbf{w}\mathbf{s} + d = 0, \forall \mathbf{s} \in \mathcal{S}$. Similarly, we find correspondences between \mathcal{F}^{i_p} and \mathcal{M}^b . Finally, we define the objective as the sum of all measurement residuals for the online calibration as

$$\begin{aligned} f_{\mathcal{M}}(\mathcal{X}) &= f_{\mathcal{M}}(\mathcal{X}_v) + f_{\mathcal{M}}(\mathcal{X}_e) \\ &= \sum_{k=p+1}^{N+1} \sum_{\mathbf{p} \in \mathcal{F}^{b_k}} \rho \left(\|\mathbf{r}(\mathbf{x}_p^{-1} \mathbf{x}_k, \mathbf{p})\|_{\Sigma_p}^2 \right) \\ &\quad + \sum_{i=2}^I \sum_{\mathbf{p} \in \mathcal{F}^{i_p}} \rho \left(\|\mathbf{r}(\mathbf{x}_{l_i}^b, \mathbf{p})\|_{\Sigma_p}^2 \right), \end{aligned} \quad (21)$$

where $\mathbf{x}_p^{-1} \mathbf{x}_k$ calculates the relative transformation from the pivot frame to the k^{th} frame.

C. Optimization With Pure Odometry

Once we finish the online calibration by fulfilling the convergence criterion (see Section VII-D), the optimization with pure odometry given accurate extrinsics is then performed. In this case, we do not optimize the extrinsics and utilize the map-based measurement from all LiDAR to improve the single-LiDAR odometry. We incorporate all constraints between

Algorithm 1: Monitoring Calibration Convergence

Input: objective $f_{\mathcal{M}}(\cdot)$, current extrinsics $\tilde{\mathbf{x}} \triangleq \mathbf{x}_{l_i}^b$
Output: optimal extrinsics $\hat{\mathbf{x}}$, covariance matrix Ξ_{calib}

```

1 Denote  $\mathcal{L}$  the set of all eligible estimates;
2 if calibration is ongoing then
3   Linearize  $f_{\mathcal{M}}$  at  $\tilde{\mathbf{x}}$  to obtain  $\Lambda = (\frac{\partial f_{\mathcal{M}}}{\partial \mathbf{x}})^\top \frac{\partial f_{\mathcal{M}}}{\partial \mathbf{x}}$ ;
4   Compute the smallest eigenvalue  $\lambda$  of  $\Lambda$ ;
5   if  $\lambda > \lambda_{calib}$  then
6     Set  $\tilde{\mathbf{x}}$  as the current extrinsics of the system;
7      $\mathcal{L} = \mathcal{L} \cup \tilde{\mathbf{x}}$ ;
8     if  $|\mathcal{L}| > \mathcal{L}_{calib}$  then
9        $\hat{\mathbf{x}} = E[\mathbf{x}]$  as the mean;
10       $\Xi_{calib} = Cov[\mathbf{x}]$  as the covariance;
11      Stop the online calibration;
12 return  $\hat{\mathbf{x}}, \Xi_{calib}$ 

```

features of all LiDARs and the corresponding local map into the cost function as

$$\begin{aligned}
f_{\mathcal{M}}(\mathcal{X}) &= f_{\mathcal{M}}(\mathcal{X}_v) \\
&= \sum_{k=p+1}^{N+1} \sum_{\mathbf{p} \in \mathcal{F}^{b_k}} \rho\left(\|\mathbf{r}(\mathbf{x}_p^{-1} \mathbf{x}_k, \mathbf{p})\|_{\Sigma_p}^2\right) \\
&\quad + \sum_{i=2}^I \sum_{k=p+1}^{N+1} \sum_{\mathbf{p} \in \mathcal{F}^{l_i}} \rho\left(\|\mathbf{r}(\mathbf{x}_p^{-1} \mathbf{x}_k \mathbf{x}_{l_i}^b, \mathbf{p})\|_{\Sigma_p}^2\right),
\end{aligned} \tag{22}$$

where $\mathbf{x}_p^{-1} \mathbf{x}_k \mathbf{x}_{l_i}^b$ is the transformation from the primary LiDAR at the pivot frame to auxiliary LiDARs at the k^{th} frame.

D. Monitoring the Convergence of Calibration

While working on the online calibration in an unsupervised way, it is of interest to decide whether calibration is converging. After the convergence, we fix the extrinsics. This is beneficial to our system since both the odometry and mapping are given more geometric constraints from auxiliary LiDARs for more accurate poses. As derived in [33], the *degeneracy factor* λ , which is the smallest eigenvalue of the *information matrix*, reveals the condition of a least-square optimization problem. Motivated by this work, we use λ to indicate whether our problem contains sufficient constraints or not for accurate extrinsics. The detailed pipeline to update extrinsics and monitor the convergence is summarized in Algorithm 1. The algorithm takes the function $f_{\mathcal{M}}(\cdot)$ defined in (21) as well as the current extrinsics as input, and produces the optimized extrinsics. On line 4, we compute λ from the information matrix of the cost function. On lines 5–7, the extrinsics are updated if λ is larger than a threshold. On line 8, we use the number of candidate extrinsics to check the convergence. On lines 9–10, the convergence criterion is met, and the termination is triggered. We then compute the sampling mean of \mathcal{L} as the resulting extrinsics and the sampling covariance as the calibration covariance.

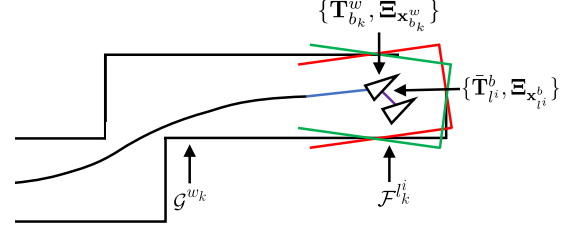


Fig. 5. Illustration of the mapping process and occurrence of noisy map points. The black curve represents historical poses. The blue curve indicates the current pose of the primary LiDAR. The purple curve shows the extrinsics from the primary LiDAR to the auxiliary LiDAR. With the pose and extrinsics, input features (red and green lines) are transformed and added into the map. But noisy transformations make new map points uncertain.

E. Marginalization

We apply the marginalization method to update states in the sliding window. We explain that the process of marginalization incorporates historical information as a prior in our optimization. Consequently, the marginalization reduces the information loss caused by discarding states. It is a critical step to maintain the consistency of calibration and odometry. Since our system does not estimate the positions of features, \mathbf{x}_p is the only state to be marginalized. By applying the Schur complement, we obtain Λ_{rr}^* and \mathbf{g}_r^* with the form of $\Lambda \delta \mathcal{X} = -\mathbf{g}$. The prior residuals are written as $\|\mathbf{r}_{pri}\|^2 = \mathbf{g}_r^{*\top} \Lambda_{rr}^{*-1} \mathbf{g}_r^*$. Please see details in Appendix B for the mathematical foundations for marginalization.

VIII. UNCERTAINTY-AWARE MULTI-LiDAR MAPPING

We first review the pipeline of the mapping module of typical LiDAR SLAM systems [16]–[18]. Taking the prior odometry as input, the algorithm constructs a global map and refines the poses with enough constraints. This is done by minimizing the sum of all map-based residual errors as:

$$\hat{\mathbf{x}}_{b_k}^w = \arg \min_{\mathbf{x}_{b_k}^w} \sum_{i=1}^I \sum_{\mathbf{p} \in \mathcal{F}^{l_i}} \rho\left(\|\mathbf{r}(\mathbf{x}_{b_k}^w \mathbf{x}_{l_i}^b, \mathbf{p})\|_{\Sigma_p}^2\right), \tag{23}$$

where \mathcal{F}^{l_i} are the input features while perceiving the k^{th} point cloud, \mathcal{G}^{w_k} is the global map, and $\mathbf{x}_{b_k}^w \mathbf{x}_{l_i}^b$ denotes the state of the i^{th} LiDAR. We use the method in Section VII-B to find correspondences between \mathcal{F}^{l_i} and \mathcal{G}^{w_k} . After solving (23), the resulting pose is used to transform current features into the world frame, and add them into the map. To reduce the computational and memory complexity, the map is also downsized using a voxel grid filter [69].

However, the precision of optimization depends on the map quality. Fig. 5 visualizes the occurrence of noisy map points transformed by the uncertain pose. We believe that several sources of uncertainty make map points noisy, and they should be addressed. Except for the sensor noise introduced in Section III-B, we identify the following uncertainties during mapping:

- **Degenerate Pose Estimation** arises from cases such as lack of geometrical structures in poorly constrained environments [33]. It typically makes poses uncertain in their degenerate directions. Existing works resort to

model-based [70]–[72] and learning-based [73] methods to estimate pose covariances in the context of ICP.

- **Extrinsic Perturbation** always exists due to calibration error [12], or vibration, impact, and temperature drift during long-term operation. Especially for wide baseline sensors such as stereo cameras, they suffer even more extrinsic deviations than the normal one. Such perturbation is detrimental to the measurement accuracy [74] for multi-sensor systems but is hard to measure.

In the next section, we first provide several preliminaries to associate uncertainties with transformation matrices. We then use these tools to model the uncertainties of measurements, poses, and extrinsics. These uncertainties are expressed as covariance matrices, and they are passed through transformations and propagated on map points. As a result, each map point is modeled as an i.i.d Gaussian variable. Finally, we propose an uncertainty-aware approach to improve the robustness and accuracy of the multi-LiDAR mapping algorithm.

A. Uncertainty Estimation and Propagation

We employ the method and notations in [19] to model data uncertainty. We assume all noises from LiDAR measurements, pose estimation, and extrinsics to be Gaussian. We first represent a noisy LiDAR point in *homogeneous coordinates* as:

$$\mathbf{p} = \bar{\mathbf{p}} + \mathbf{D}\boldsymbol{\zeta}, \quad \boldsymbol{\zeta} \sim \mathcal{N}(\mathbf{0}, \mathbf{Z}), \quad (24)$$

where

$$\mathbf{p} = [x, y, z, 1]^\top, \quad (25)$$

where $\bar{\mathbf{p}}$ is a noise-free value, $\boldsymbol{\zeta} \in \mathbb{R}^3$ is a small Gaussian perturbation variable with zero mean, \mathbf{Z} is noise covariance defined in Section III-B, and \mathbf{D} is a matrix that converts a 3×1 vector into *homogeneous coordinates* [19]. We also define a random variable in $SE(3)$ with a small perturbation as:

$$\mathbf{T} = \exp(\boldsymbol{\xi}^\wedge) \bar{\mathbf{T}}, \quad \boldsymbol{\xi} \sim \mathcal{N}(\mathbf{0}, \boldsymbol{\Xi}), \quad (26)$$

where $\bar{\mathbf{T}}$ is a noise-free transformation and $\boldsymbol{\xi} \in \mathbb{R}^6$ is the small perturbation variable with covariance $\boldsymbol{\Xi}$. This representation allows us to store the mean transformation as $\bar{\mathbf{T}}$ and use $\boldsymbol{\xi}$ for perturbation on the vector space. We now represent the covariances of poses and extrinsics.

The poses are optimized through the least-squares method, as derived in (6). We directly calculate the inverse of the *information matrix* i.e. $\boldsymbol{\Xi}_{\mathbf{x}_{b_k}^w} = \boldsymbol{\Lambda}^{-1}$, as the pose covariances. The setting of the extrinsic covariances depends on a specific situation. We generally define the extrinsic covariance as:

$$\boldsymbol{\Xi}_{\mathbf{x}_{l_i}^b} = \alpha \cdot \boldsymbol{\Xi}_{calib}, \quad \boldsymbol{\xi}_{l_i}^b \sim \mathcal{N}(\mathbf{0}, \boldsymbol{\Xi}_{\mathbf{x}_{l_i}^b}), \quad (27)$$

where $\boldsymbol{\xi}_{l_i}^b$ is the perturbation variable of extrinsics, $\boldsymbol{\Xi}_{calib}$ is the calibration covariance calculated according to Algorithm 1, and α is a scaling parameter allowing us to increase the magnitude of the covariance. If a multi-LiDAR system was calibrated just now, we set $\alpha = 1$. If the system has been used for a long time and not re-calibrated, there should be small extrinsic deviations on LiDARs, and α is set to be larger. Given the mean pose of the base sensor, the mean extrinsics, and their covariances, we then compute the mean poses of

other LiDARs and the covariances i.e. $\{\mathbf{T}_{l_k}^w, \boldsymbol{\Xi}_{l_k}^w\}$. This is a problem about compounding two noisy poses, and we follow the fourth-order approximation in [19] to calculate them.

We need to pass the Gaussian uncertainty of a point through a noisy transformation to produce a mean and covariance for its new measurement in the map $\{\mathbf{y}, \boldsymbol{\Sigma}\}$. By transforming a point into the world frame, we have

$$\begin{aligned} \mathbf{y} &\triangleq \mathbf{T}_{l_k}^w \mathbf{p} = \exp(\boldsymbol{\xi}_{l_k}^{w\wedge}) \bar{\mathbf{T}}_{l_k}^w (\bar{\mathbf{p}} + \mathbf{D}\boldsymbol{\zeta}) \\ &\approx (\mathbf{I} + \boldsymbol{\xi}_{l_k}^{w\wedge}) \bar{\mathbf{T}}_{l_k}^w (\bar{\mathbf{p}} + \mathbf{D}\boldsymbol{\zeta}), \end{aligned} \quad (28)$$

where we keep the first-order approximation of the exponential map. If we multiply out the equation and retain only the first-order terms, we have

$$\mathbf{y} \approx \mathbf{h} + \mathbf{H}\boldsymbol{\theta}, \quad (29)$$

where

$$\begin{aligned} \mathbf{h} &= \bar{\mathbf{T}}_{l_k}^w \bar{\mathbf{p}}, \quad \mathbf{H} = [(\bar{\mathbf{T}}_{l_k}^w \bar{\mathbf{p}})^\odot \quad \bar{\mathbf{T}}_{l_k}^w \mathbf{D}], \\ \boldsymbol{\theta} &= \begin{bmatrix} \boldsymbol{\xi}_{l_k}^w \\ \boldsymbol{\zeta} \end{bmatrix}, \quad \boldsymbol{\theta} \sim \mathcal{N}(\mathbf{0}, \boldsymbol{\Theta}), \quad \boldsymbol{\Theta} = \text{diag}(\boldsymbol{\Xi}_{l_k}^w, \mathbf{Z}), \end{aligned} \quad (30)$$

where \odot converts a 4×1 columns into a 4×6 matrix as

$$\begin{bmatrix} \boldsymbol{\varepsilon} \\ \boldsymbol{\eta} \end{bmatrix}^\odot = \begin{bmatrix} \eta \mathbf{I} & -\boldsymbol{\varepsilon}^\wedge \\ \mathbf{0}^\top & \mathbf{0}^\top \end{bmatrix}, \quad \boldsymbol{\varepsilon} \in \mathbb{R}^3, \quad \eta = 1, \quad (31)$$

where all perturbation variables are embodied into $\boldsymbol{\theta}$ in \mathbb{R}^9 . The covariance $\boldsymbol{\Theta} = \text{diag}(\boldsymbol{\Xi}_{l_k}^w, \mathbf{Z})$ denotes the combined uncertainties of sensor readings, estimated poses, and extrinsics. Obviously, \mathbf{y} is also Gaussian with the mean $\bar{\mathbf{y}}$ and propagated covariance $\boldsymbol{\Sigma}$ as

$$\bar{\mathbf{y}} = \mathbf{h}, \quad \boldsymbol{\Sigma} = \mathbf{H}\boldsymbol{\Theta}\mathbf{H}^\top, \quad (32)$$

where we follow [75] to use the trace, i.e., $\text{tr}(\boldsymbol{\Sigma})$, to quantify the magnitude of a covariance.

B. Uncertainty-Aware Operation

The original mapping algorithm is integrated with three additional steps to boost its performance and robustness. From the last section, we show that the covariances of all map points can be correctly propagated by considering the above error sources. This operation lets the cost function take the pose uncertainty and extrinsic perturbation into account. As a result, a point that stays near the origin should have a high weight. And the primary LiDAR tends to have more confidence than auxiliary LiDARs given the extrinsic covariances.

Second, before adding points into the global map, we remove outliers if $\text{tr}(\boldsymbol{\Sigma})$ is larger than a threshold. Finally, we modify the original voxel grid filter to downsize the global map in a probabilistic way. The modified filter samples points for each cube according to their covariances. Let $\{\mathbf{y}_i, \boldsymbol{\Sigma}_i\}$ be the i^{th} point in a cube, and m be the number of points in the cube. The sampled mean and covariance of a cube are:

$$\bar{\mathbf{y}} = \sum_{i=1}^M w_i \mathbf{y}_i, \quad \boldsymbol{\Sigma} = \sum_{i=1}^M w_i^2 \boldsymbol{\Sigma}_i, \quad (33)$$

where w is the threshold, and $w_i = \frac{w - \text{tr}(\boldsymbol{\Sigma}_i)}{\sum_{i=1}^m [w - \text{tr}(\boldsymbol{\Sigma}_i)]}$ is a normalized weight.

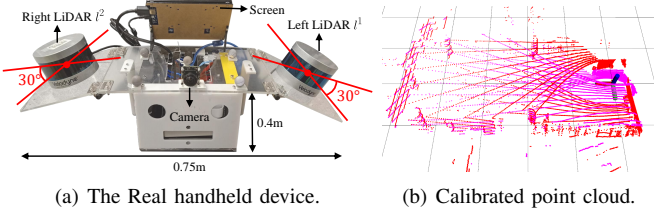


Fig. 6. (a) The real handheld device for indoor tests. Two VLP-16s are mounted at the left and right sides respectively. The attached camera is used to record test scenes. (b) The calibrated point cloud consists of points from the left (red) and right (pink) LiDARs.

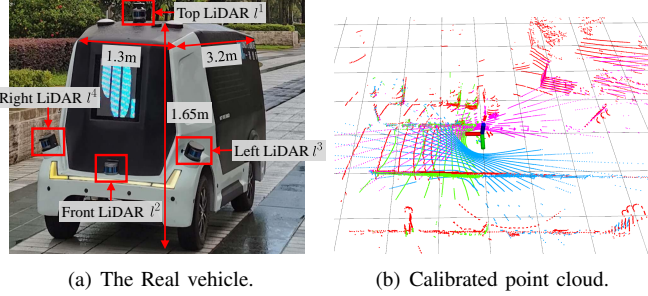


Fig. 7. (a) The real vehicle for large-scale, outdoor tests. Four RS-16s are mounted at the top, front, left, and right position respectively. (b) The calibrated point cloud consists of points from the top (red), front (green), left (blue), and right (pink) LiDARs.

IX. EXPERIMENT

We perform simulated and real-world experiments on three platforms to test the calibration and SLAM performance of the proposed M-LOAM. First, we calibrate multi-LiDAR systems for all presented platforms. The proposed algorithm is compared with SOTA methods, and two metrics are introduced for evaluation. Second, we demonstrate the SLAM performance of M-LOAM in various scenarios covering indoor environments and outdoor urban roads. Moreover, to evaluate the sensibility of M-LOAM against extrinsic error, we test M-LOAM on the handheld device and vehicle under different-level extrinsic perturbation. Finally, we provide a study to comprehensively evaluate M-LOAM's performance and computation time with various LiDAR combinations.

A. Implementation Details

The PCL library [69] is used to process point clouds. The Ceres Solver [76] is used to solve nonlinear problems. During experiments, our algorithm is executed on a computer with an Intel i7-7700K CPU at 4.20 GHz and 32 GB memory. Three platforms with different multi-LiDAR systems, including a simulated robot, a handheld device, and a vehicle are tested.

- **The Simulated Robot (SR)** is built on the Gazebo [77]. Two 16-beam LiDARs are mounted on a mobile robot for testing. We build a closed simulated rectangular room. We use the approach from [78] to set the LiDAR configuration for maximizing the sensing coverage. We moved the robot in the room at an average speed of $0.5m/s$. The ground-truth extrinsics and poses are provided.

TABLE II
PARAMETERS FOR CALIBRATION AND SLAM.

σ_R	λ_{calib}	\mathcal{L}_{calib}	N	p	w	α
0.25	70	25	4	2	100	≥ 1

- **The Real Handheld Device (RHD)** is made for handheld tests and shown in Fig. 6. Its configuration is similar to that of the SR. Besides VLP-16s³, we also install a mini computer (Intel NUC) for data collection and a camera (mvBlueFOX-MLC200w) for recording test scenes. We used this device to collect data on the campus with an average speed of $2m/s$.
- **The Real Vehicle (RV)** is a vehicle for autonomous logistic transportation [11]. We conduct experiments on this platform to demonstrate that our system also performs well in large-scale, challenging outdoor environments. As shown in Fig. 7, four RS-LiDAR-16s⁴ are rigidly mounted at the top, front, left, and right positions respectively. We drove the vehicle through urban roads at an average speed of $3m/s$. Ground-truth poses are obtained from a coupled LiDAR-GPS-encoder localization system that was proposed in [79], [80].

Table II shows the parameters which are empirically set in the system. σ_R , λ_{calib} , and \mathcal{L}_{calib} are the calibration convergence thresholds. Setting the last two parameters need a preliminary training process, which is detailed in the supplementary material [81]. p is the size of the local map, and N is the size of the sliding window in odometry. w is the threshold of filtering uncertain points in mapping. α is the scale of the extrinsic covariance. We set $\alpha = 10$ for the case of injecting large perturbation in Section IX-D. Otherwise, $\alpha = 1$.

B. Performance of Calibration

1) *Evaluation Metrics:* We introduce two metrics to assess the LiDAR calibration results from different aspects:

- **Error Compared With Ground truth (EGT)** computes the distance between the ground truth and the estimated values in terms of rotation and translation as

$$\begin{aligned} EGT_R &= \|\ln(R_{gt}R_{est}^{-1})^\vee\|, \\ EGT_t &= \|\mathbf{t}_{gt} - \mathbf{t}_{est}\|, \end{aligned} \quad (34)$$

- **Mean Map Entropy (MME)** is proposed to measure the compactness of a point cloud [82]. It has been explored as a standard metric to assess the quality of different registration algorithms [83]. Given a calibrated point cloud, the normalized mean map entropy is

$$MME = \frac{1}{m} \sum_{i=1}^m \ln[\det(2\pi e \cdot \mathbf{C}_{\mathbf{p}_i})], \quad (35)$$

where m is the size of the point cloud and $\mathbf{C}_{\mathbf{p}_i}$ is the sampling covariance within a local radius r around \mathbf{p}_i . For each calibration case, we select 10 consecutive frames

³<https://velodynelidar.com/products/puck>

⁴<https://www.robosense.ai/rslidar/rs-lidar-16>

TABLE III
CALIBRATION RESULTS. \downarrow INDICATES THAT THE LOWER VALUE, THE BETTER SCORE.

Case	Method	Rotation [deg]			Translation [m]			EGT_R [deg, \downarrow]	EGT_t [m, \downarrow]	\overline{MME} [\downarrow]	
		x	y	z	x	y	z			$r = 0.3m$	$r = 0.4m$
SR1 (Left-Right)	Auto-Calib	6.134	1.669	0.767	0.001	-0.635	-0.083	33.911	0.209	-2.016	-2.463
	Proposed (Ini.)	44.154	7.062	1.024	-0.027	-0.719	0.000	8.229	0.328	-2.240	-2.685
	Proposed (Ini.+Ref.)	40.870	0.397	0.237	-0.012	-0.475	-0.206	0.997	0.018	-2.690	-3.073
	PS-Calib	40.021	-0.005	-0.010	0.001	-0.476	-0.218	0.037	0.003	-2.730	-3.115
	W/O Calib	0.000	0.000	0.000	0.000	0.000	0.000	40.000	0.525	-2.358	-2.704
	GT	40.000	0.000	0.000	0.000	-0.477	-0.220	—	—	-2.733	-3.111
SR2 (Left-Right)	Auto-Calib	4.680	-1.563	0.647	0.032	-0.751	-0.022	35.337	0.339	-2.336	-2.447
	Proposed (Ini.)	40.854	3.517	0.285	-0.019	-0.667	0.000	3.632	0.291	-2.607	-2.804
	Proposed (Ini.+Ref.)	38.442	0.111	-0.037	0.000	-0.504	-0.205	1.549	0.030	-3.016	-3.192
	PS-Calib	40.021	-0.005	-0.010	0.001	-0.476	-0.218	0.0365	0.003	-3.113	-3.306
	W/O Calib	0.000	0.000	0.000	0.000	0.000	0.000	40.000	0.525	-2.875	-2.878
	GT	40.000	0.000	0.000	0.000	-0.477	-0.220	—	—	-3.117	-3.313
RHD (Left-Right)	Auto-Calib	7.183	-3.735	33.329	0.653	-2.006	-0.400	44.312	1.612	-3.612	-2.711
	Proposed (Ini.)	36.300	0.069	-3.999	0.113	-0.472	-0.103	6.443	0.112	-3.664	-2.839
	Proposed (Ini.+Ref.)	37.545	-0.376	0.773	0.066	-0.494	-0.113	2.491	0.064	-3.681	-2.862
	CAD Model	40.000	0.000	0.000	0.000	-0.456	-0.122	2.077	0.092	-3.662	-2.833
	W/O Calib	0.000	0.000	0.000	0.000	0.000	0.000	40.000	0.560	-3.696	-2.868
	PS-Calib	39.629	-1.664	1.193	0.033	-0.540	-0.142	—	—	-3.696	-2.868
RV (Top-Front)	Auto-Calib	-19.634	21.610	-3.481	-0.130	-0.282	-0.850	22.852	0.791	-2.705	-2.282
	Proposed (Ini.)	1.320	7.264	3.011	-0.324	0.227	0.000	3.217	1.433	-2.721	-2.332
	Proposed (Ini.+Ref.)	-2.057	6.495	2.133	0.528	-0.036	-1.102	0.274	0.081	-2.885	-2.370
	CAD Model	0.000	10.000	0.000	0.795	0.000	-1.364	4.505	0.351	-2.771	-2.312
	W/O Calib	0.000	0.000	0.000	0.000	0.000	0.000	7.227	1.252	-2.785	-2.306
	PS-Calib	-1.817	6.629	2.134	0.536	0.039	-1.131	—	—	-2.902	-2.416

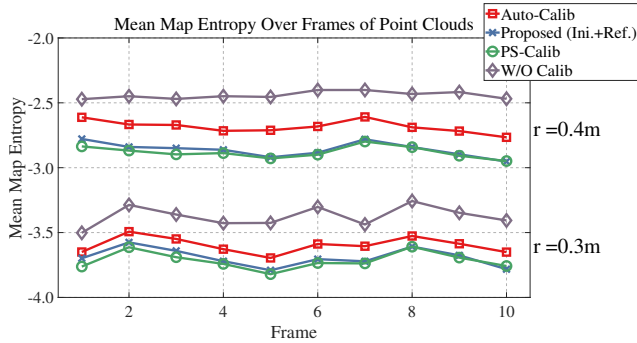


Fig. 8. The MME values over 10 consecutive frames of point clouds which are calibrated by different approaches on the RHD platform. The lower entropy means the better score of a method.

of point clouds that contain many planes and compute their average MME values for evaluation.

Since the perfect ground truth is unknown in real-world applications, we use the results of **PS-Calib** [12] as the “relative ground truth” to compute the EGT metric. PS-Calib is a well-understood, target-based calibration approach, which should have the similar or superior accuracy to our method [84]. Another metric is the MME, which computes the score in an unsupervised way. It can be interpreted as an information-theoretic measure of the compactness of a point cloud.

2) *Calibration Results*: The multi-LiDAR systems of all the presented platforms are calibrated by our methods. To

initialize the extrinsics, we manually move these platforms with sufficient rotations and translations. We compare our method with **Auto-Calib** [4] which is an offline multi-LiDAR calibration approach. Although Auto-Calib follows the similar initialization-refinement procedure to obtain the extrinsics, it is different from our algorithm in many details. For example, Auto-Calib only uses the planar constraints in refinement. And it assumes that LiDARs’ views should have large overlapping regions. The results using the initial (**Initialization**), uncalibrated (**W/O Calib**), **CAD model**, and ground-truth (**GT**) extrinsics are also provided for reference. Table III reports the calibration results, where two simulated cases (same extrinsics, different motions) and two real-world cases are tested. Due to space limitation, we only show the calibration between the top LiDAR and front LiDAR on the vehicle.

Our hand-eye-based initialization successfully obtain the rotation offset ($< 9deg$) for all cases, but fails to recover the translation offset ($> 0.3m$) except for the RHD. Both the SR and RV have to perform planar movement with a long distance for initialization, making the recovery of the x -, y - translation is poor due to the drift of motion estimation. Also the z - translation is not observable. But the RHD can perform 6-DoF movements and rapidly gather rich constraints. Its initialization results are thus good. Regarding the online refinement, our algorithm outperforms Auto-Calib and demonstrates comparable performance with PS-Calib in terms of the EGT ($< 3deg$ and $< 0.07m$) and MME metrics.

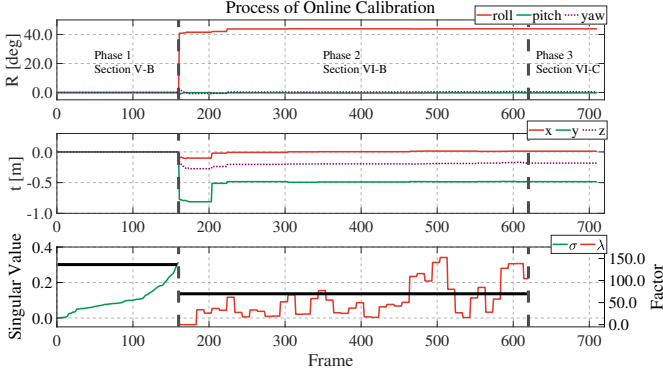


Fig. 9. Detailed illustration of the whole calibration process, including the initialization and optimization with online calibration on the RHD. Different phases are separated by the bold dashed lines. In Phase 1, the initial rotation and translation are estimated with the singular value-based exit criteria (Section VI-B). In Phase 2, the nonlinear optimization-based calibration refinement process is performed. The convergence is determined by the *degeneracy factor* (Section VII-D). Phase 3 only optimizes the LiDAR odometry with fixed extrinsics. The black lines in the bottom plot indicate the setting thresholds σ_R and λ_{calib} which are defined in previous sections.

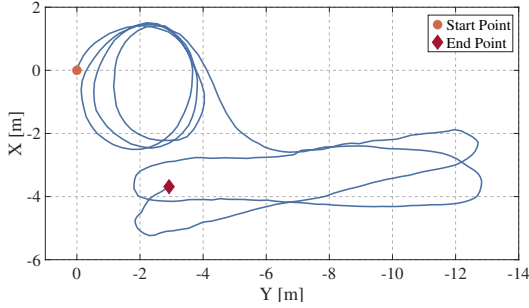


Fig. 10. Calibration trajectory of the sensor suite estimated by M-LO on the RHD. The dot and diamond indicate the start and end point respectively.

Based on these results, we conclude that the initialization phase can provide coarse rotation estimates, and the refinement for precise extrinsics is required.

We explicitly show the test on the RHD in detail. In Fig. 8, we plot all MME values over different frames of calibrated point clouds, where the results are consistent with Table III. Whether r is set to $0.3m$ or $0.4m$, our method always has a better score than Auto-Calib. Fig. 9 illustrates all phases of the calibration process on the RHD, with the trajectory of the sensor suite shown in Fig. 10. The calibration starts with recovering the rotational offsets (Phase 1, Section VI-B) without prior knowledge about the mechanical configuration. Phase 1 exits when the second small singular values of \mathbf{Q}_K are larger than a threshold. The translational components are then computed. Phase 2 (Section VII-B) performs a nonlinear optimization to jointly refine the rotation and translation. This process may last for a prolonged period if there are no sufficient environmental constraints. However, our sliding window-based marginalization scheme ensures a bounded-complexity program to consistently update the extrinsics. The convergence condition is monitored with the *degeneracy factor* (Section VII-D). After that, the calibration is turned off, and we enter phase 3 for pure odometry (Section VII-C) and mapping (Section VIII) which are evaluated in Section IX-C.

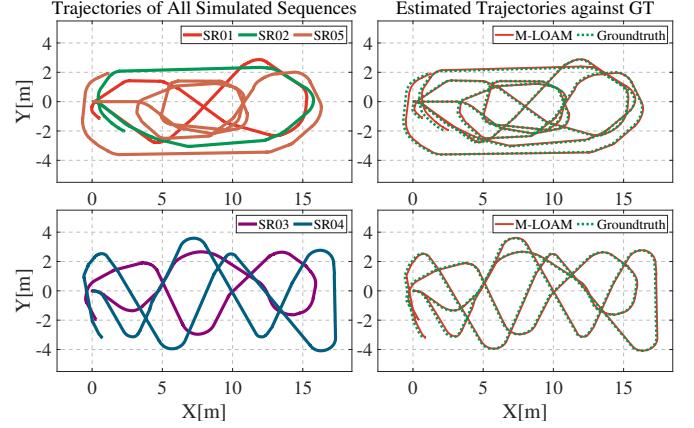


Fig. 11. (Left) Trajectories of the *SR01-SR05* sequences with different lengths. (Right) M-LOAM's trajectories compared against the ground truth.

TABLE IV
ATE [85] ON SIMULATED SEQUENCES

Metric	Sequence	Length	M-LO	M-LOAM -wo-ua	M-LOAM	A-LO	A-LOAM
RMSE_t [m]	<i>SR01easy</i>	40.6m	0.482	0.041	0.041	2.504	0.060
	<i>SR02easy</i>	39.1m	0.884	0.034	0.034	3.721	0.060
	<i>SR03hard</i>	49.2m	0.838	0.032	0.032	4.738	0.059
	<i>SR04hard</i>	74.2m	0.757	0.032	0.032	2.083	0.388
	<i>SR05hard</i>	81.2m	0.598	0.033	0.033	4.841	0.208
RMSE_R [deg]	<i>SR01easy</i>	40.6m	3.368	0.824	0.676	26.484	0.751
	<i>SR02easy</i>	39.1m	7.971	1.070	0.882	37.903	0.576
	<i>SR03hard</i>	49.2m	6.431	0.994	0.865	38.923	0.750
	<i>SR04hard</i>	74.2m	5.728	0.919	0.772	21.027	0.711
	<i>SR05hard</i>	81.2m	6.509	0.754	0.554	87.999	2.250

We also evaluate the sensitivity of our refinement method to different level of initial guesses: the CAD model as well as rough rotational and translational initialization. Quantitative results can be found in the supplementary material [81].

C. Performance of SLAM

We evaluate M-LOAM on both simulated and real-world sequences which are collected by the SR, RHD, and RV platforms. The multi-LiDAR systems are calibrated with our online approach (see Section VII-B). The detailed extrinsics can be found on the first, third, and fourth row in Table III. We compare M-LOAM with two SOTA, open-source LiDAR-based algorithms: **A-LOAM**⁵ (the advanced implementation of LOAM [16]) and **LEGO-LOAM** [17]. Both of them directly take the calibrated and merged point clouds as input, while our approach employs the optimization-based method to fuse point clouds. There are many differences in details among these methods, as presented in the technical sections. Our system is complete with online calibration as well as uncertainty estimation. Since LEGO-LOAM is a ground-optimized system and requires LiDARs to be horizontally installed, its results are only provided on the RV sequences for a fair comparison.

⁵<https://github.com/HKUST-Aerial-Robotics/A-LOAM>

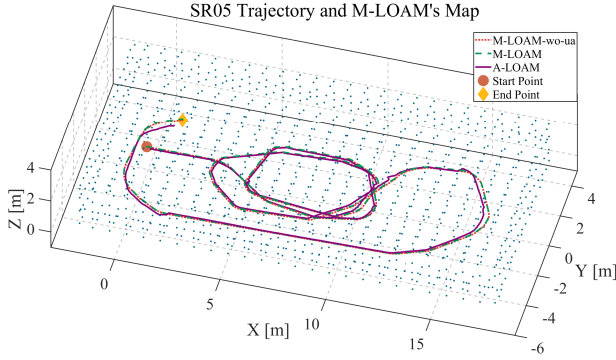


Fig. 12. Trajectories on *SR05* of M-LOAM-wo-ua, M-LOAM, and A-LOAM and the map constructed by M-LOAM. A-LOAM has a few defects, while M-LOAM-wo-ua's trajectory nearly overlaps with that of M-LOAM.

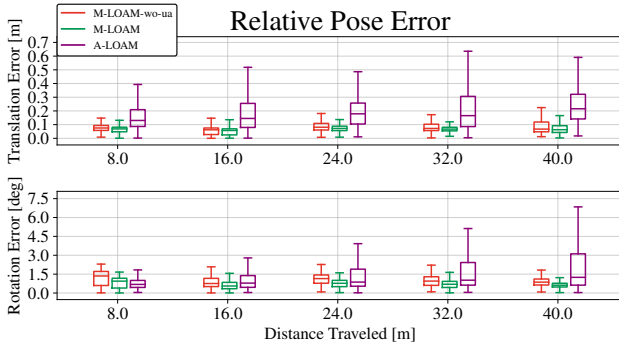
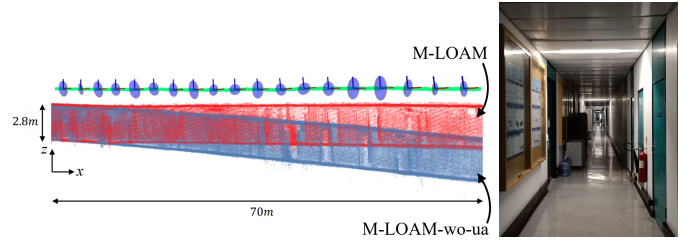


Fig. 13. The mean RPE on *SR05* with 10 trials. For the distance: 40m, the median values of the relative translation and rotation error of M-LOAM-wo-ua, M-LOAM, and A-LOAM are (0.87deg, 0.07m), **(0.62deg, 0.06m)**, (1.26deg, 0.22m) respectively.

The results estimated by parts of M-LOAM are also provided. These are denoted by **M-LO** and **M-LOAM-wo-ua**, indicating our proposed odometry (Section VII-C) and the complete M-LOAM without the awareness of uncertainty (Section VIII-B), respectively. To fulfill the real-time requirement, we run the odometry in 10-Hz and the mapping in 5-Hz.

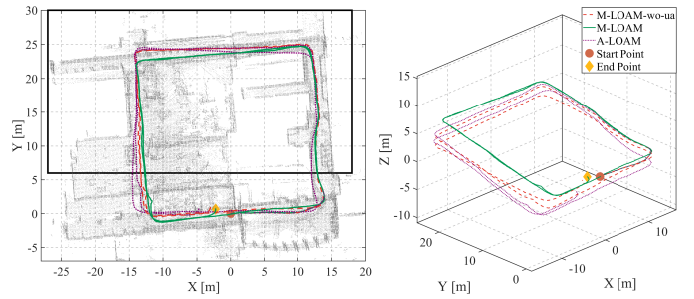
1) *Simulated Experiment*: We move the SR to follow 5 paths with the same start point to verify our proposed method. Each sequence is performed with 10-trial SLAM tests, and at each trial, the point clouds are post-processed by adding zero-mean Gaussian noises with an std of 0.05m. The ground-truth and the estimated trajectories of M-LOAM are plotted in Fig. 11. The absolute trajectory error (ATE) on all sequences is shown in Table IV, as evaluated in terms of root-mean-square error (RMSE) [85]. All sequences are split into either an *easy* or *hard* level according to their length.

First, M-LO outperforms A-LO around 4 – 10 orders of magnitudes, which shows that the sliding window estimator can refine the frame-to-frame odometry. Second, we observe that the mapping module greatly refines the odometry module. Third, M-LOAM outperforms other methods in most of the cases. This is due to two main reasons. 1) The small calibration error may potentially affect the map quality and degrade M-LOAM-wo-ua and A-LOAM performance. 2) The estimates from A-LO do not provide a good prior to A-LOAM. Since the robot has to turn around in the room for exploration, A-



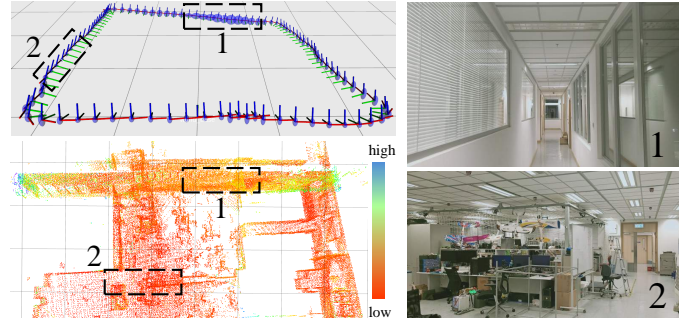
(a) Visualization of poses and maps with covariances. (b) Scene image.

Fig. 14. (a) Side view of sample poses with covariances estimated by M-LOAM and generated map on *RHD01corridor*. The below blue map is created by M-LOAM-wo-ua. The upper red map is created with M-LOAM. The covariances of pose calculated by M-LOAM are visualized as blue ellipses. A large radius represents a high uncertainty of a pose. The pose estimates in the x -, z - direction are degenerate and uncertain, making the map points on the ceiling and ground noisy. M-LOAM is able to maintain the map quality by smoothing the noisy points. (b) The scene image.



(a) Map and trajectories.

(b) Trajectories.



(c) Pose and map points with uncertainties.

(d) Scene images.

Fig. 15. Results on *RHD02lab*. (a) Map generated in a laboratory and estimated trajectories (from right to left). The black box is the region shown in below figures. Two loops are in this sequence. (b) Trajectories are shown with a clearer view. (c) Visualization of the pose and map point uncertainty, where the grid size is 5m. The covariance of a pose is represent as a blue ellipse. The larger radius, the higher uncertainty. The uncertainty of a point is measured by the trace of its covariance. The larger trace, the higher uncertainty. Two marked regions indicate the degenerate (scene 1) and well-conditioned (scene 2) pose estimation respectively. With compounded uncertainty propagation, the map points in scene 1 become uncertain. (d) Scene images.

LOAM's mapping error is accumulated rapidly and further makes the optimized poses worse. This explains why A-LOAM has large error in *SR04hard* and *SR05hard*. One may argue that A-LOAM has less rotational error than other methods on *SR02easy-SR04hard*. We explain that A-LOAM uses ground points to constrain the roll and pitch angles, while M-LOAM tends to filter them out.

We show the results of *SR05hard* in detail. The estimated

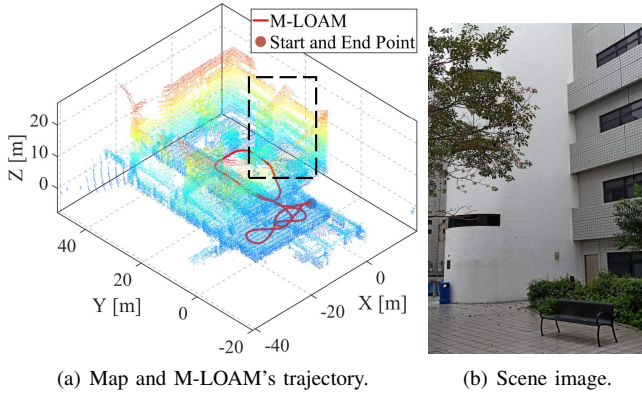


Fig. 16. Results of *RHD03garden*. (a) Map generated in a garden, and the trajectory estimated by M-LOAM. The colors of the points vary from blue to red, indicating the altitude changes (0m to 23m) (b) Scene images.

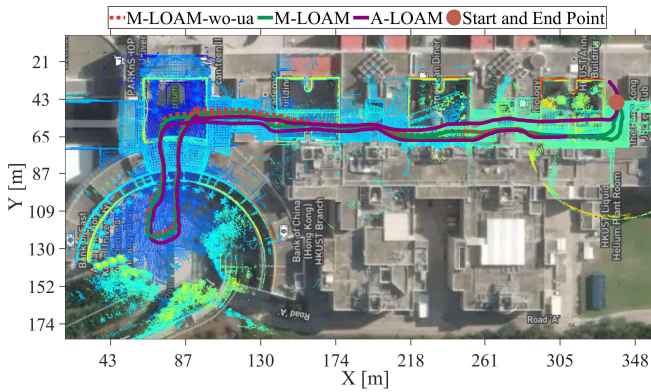


Fig. 17. Mapping results of *RHD04building* that goes through the HKUST academic buildings and the trajectories estimated by different methods (total length is 700m). The map is aligned with Google Maps. The colors of the points vary from blue to red, indicating the altitude changes (0m to 40m)

trajectories are shown in Fig. 12, where we zoom in the bounding box region for more details. A-LOAM has a few defects in the marked box region and at the tail of their trajectories, while M-LOAM-wo-ua's trajectory nearly overlaps with that of M-LOAM. The relative pose errors (RPE) evaluated by [85] are shown in Fig. 13. In this plot, M-LOAM has lower rotation and translation errors than others over a long distance.

2) *Indoor Experiment*: We used the handheld device to collect four sequences called *RHD01corridor*, *RHD02lab*, *RHD03garden*, and *RHD04building* to test our approach.

The first experiment is done in a long and narrow corridor. As emphasized in [70], this is a typical poorly-constrained environment. Here we show that the uncertainty-aware module is beneficial to our system. In Fig. 14, we illustrate the sample poses of M-LOAM and the generated map on *RHD01corridor*. The ellipses represent the size of the pose covariances. A large radius indicates that the pose in x -, z - directions of each mapping operation is uncertain. This is mainly caused that only a small set of points scan the walls and ceiling and cannot provide enough constraints. Points also become uncertain due to noisy transformations. The uncertainty-aware operation of M-LOAM is able to keep more and more certain points in the map and thus improves the precision of poses. This is the

TABLE V
MEAN RELATIVE POSE DRIFT

Sequence	Length	M-LO	M-LOAM -wo-ua	M-LOAM	A-LO	A-LOAM
<i>RHD02</i>	197m	3.82%	0.29%	0.07%	14.18%	1.13%
<i>RHD03</i>	164m	0.88%	0.029%	0.044%	5.31%	0.32%
<i>RHD04</i>	695m	7.30%	0.007%	0.003%	34.02%	6.03%

reason why M-LOAM performs better than M-LOAM-wo-ua.

We conduct more experiments to demonstrate the performance of M-LOAM on other RHD sequences comprehensively. For evaluation, these datasets contain at least a closed loop. Our results of *RHD02lab* are shown in Fig. 15. This sequence contains two loops. Fig. 15(a) shows a map built in a lab region, and Fig. 15(b) shows the trajectories estimated by different methods. Both M-LOAM-wo-ua and A-LOAM accumulates significant drift at the x -, y -, z - directions after two loops, while M-LOAM's results are almost drift free. Fig. 15(c) shows the estimated poses and map points in the first loop. The covariances of the poses and points evaluated by M-LOAM are visible as either ellipses or colored dots in the figure. Except for the corridor in scene 1, we also mark the well-conditioned environment in scene 2 for comparison. Fig. 15(d) shows the scene pictures. The results fit our previous explanation that the points in scene 1 are uncertain because of noisy poses. In contrast, scene 2 has more constraints for estimating poses, making the map points certain.

Fig. 16 shows the results of *RHD03garden*. Since the installation of LiDARs on the RHD has a large roll angle, the areas over a 20m height are scanned. Another experiment is carried out in a longer sequence. This dataset lasts for 12 minutes, and the total length is about 700m. The estimated trajectories and M-LOAM's map are aligned with Google Map in Fig. 17. Both M-LOAM-wo-ua and M-LOAM provide more accurate and consistent results than A-LOAM.

Finally, we evaluate the pose drift of results with 10 repeated trials on *RHD02*–*RHD04*. We employ the point-to-plane ICP [20] to measure the distance between the start and end point. This ground truth distance is used to compare with that of the estimates, and the calculated mean relative drift is listed Table V. Both M-LOAM-wo-ua and M-LOAM achieve a similar accuracy on *RHD03* and *RHD04* since the surroundings of these sequences are almost well-conditioned. We conclude that the uncertainty-aware operation is not really necessary in well-conditioned environments and well-calibrated sensors, but maximally reduces the negative effect of data uncertainties.

3) *Outdoor Experiment*: The large-scale, outdoor sequence was recorded with RV platform shown in Fig. 7. This sequence covers an area around 1100m in length and 450m in width and has 110m in height changes. The total path length is about 3.23km. The data lasts for 38 minutes, and contains the 10-Hz point clouds from four LiDARs and 25-Hz ground-truth poses. This experiment is very significant to test the stability and durability of M-LOAM.

M-LOAM's trajectory against the ground truth and the built map is aligned with Google Map in Fig. 18. We present the

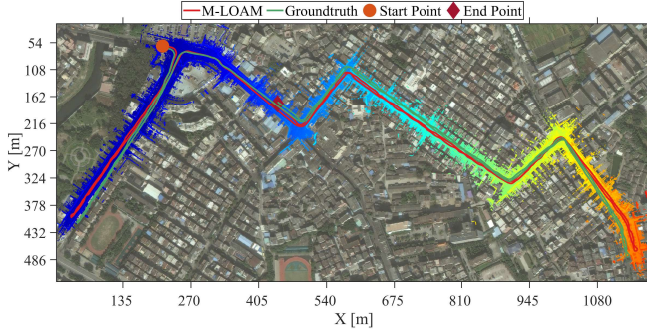


Fig. 18. Mapping results of urban road and estimated trajectory against the ground truth on the RV sequence (total length is 3.23km). The colors of the points vary from blue to red, indicating the altitude changes (0m to 200m).

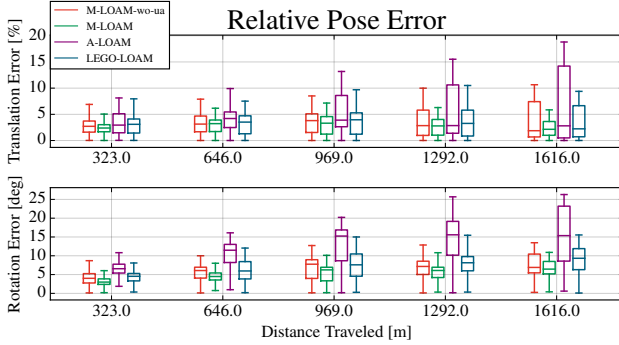
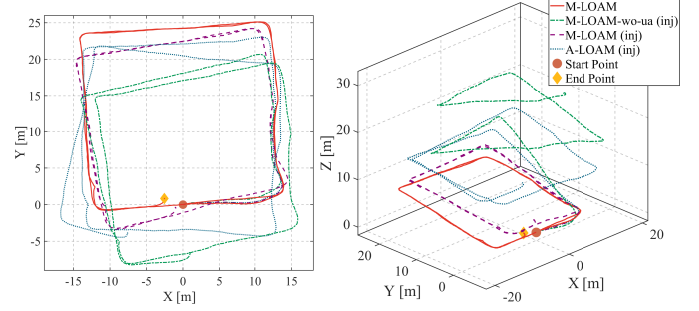


Fig. 19. RPE on the RV sequence. For the 1616m distance, the median values of the relative translation (in percentage) and rotation error of M-LOAM-wo-ua, M-LOAM, A-LOAM, and LEGO-LOAM are (6.90deg, 1.87%), (6.45deg, 2.14%), (15.36deg, 2.80%), (9.33deg, 2.23%) respectively.

RPE of M-LOAM, M-LOAM-wo-ua, A-LOAM, and LEGO-LOAM in Fig. 19. A-LOAM has the highest errors among them. Both M-LOAM-wo-ua and M-LOAM have competitive results with LEGO-LOAM. In addition, the outlier terms of M-LOAM are fewer than other methods. We thus extend our previous findings that the uncertainty-aware mapping has the capability to enhance the robustness of the system.

D. Sensitivity to Noisy Extrinsic

In this section, we evaluate the sensitivity of M-LOAM to different-level extrinsic perturbation. On the handheld and vehicle platform, we test our method by setting the extrinsics with different levels of accuracy: CAD model, initialization, and perturbation injection. The experiment setting is listed in Table VI. The injected perturbation indicates that we simulate a shock on the ground truth extrinsics with $[10, 10, 10]deg$ in roll, pitch, and yaw; $[0.1, 0.1, 0.1]m$ along x -, y -, and z - axes. We use *RHD02lab* and a small sequence on RV to compare M-LOAM with baseline methods. It should be noted that extrinsic calibration is turned off, and we only use the top and front LiDAR on RV in experiments. The estimated trajectories under the largest perturbation are shown in Fig. 20 and Fig. 21 for different platforms. These methods are marked with ‘(-inj)’. We also calculate the ATE in Table VI. Here, M-LOAM’s trajectory on *RHD02lab* in the last section is used to compute the error. From the tables and figures,



(a) Trajectories in a down view. (b) Trajectories in another view.

Fig. 20. Trajectories on *RHD02lab* with being injected by a large extrinsic perturbation. The detailed settings are shown in Table VI.

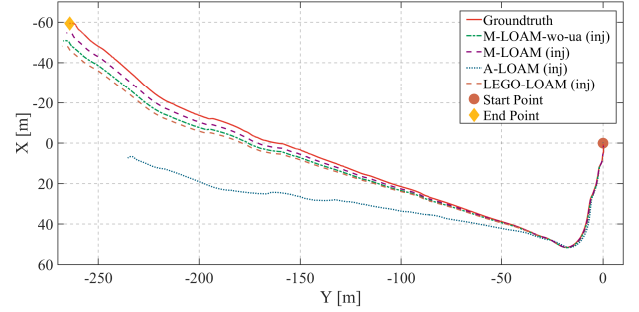


Fig. 21. Trajectories on 341m length sequence (a part of the RV sequence) with being injected by a large extrinsic perturbation. The detailed settings are shown in Table VI.

we observe that all methods’ performance is degraded along with the increasing extrinsic perturbation. But both M-LOAM-wo-ua and M-LOAM have a smaller error. Especially in the largest perturbation, M-LOAM is much more robust since it can consistently track sensors’ poses.

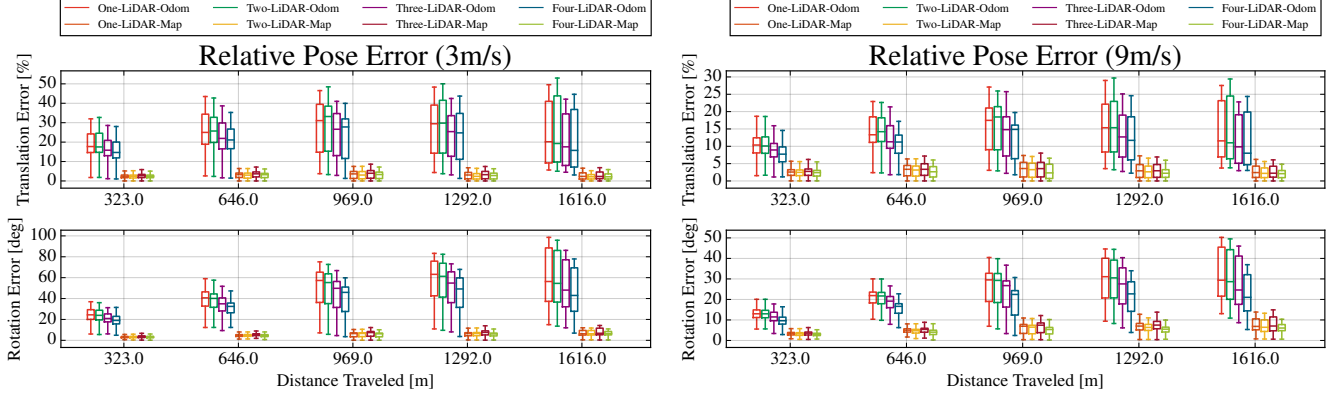
E. Single LiDAR v.s. Multiple LiDARs

In this section, we explore the specific improvements in utilizing more LiDARs in M-LOAM. The vehicle platform has four LiDARs. We use One-, Two-, Three-, Four-LiDAR to denote the setups of l^1 , $l^{1,2}$, $l^{1,2,3}$, and $l^{1,2,3,4}$ respectively. We also use x-Odom and x-Map to denote results provided by the odometry and mapping using different setups, respectively. The tests are carried out on the complete RV sequence. We first report statistics of the program in Table VII, including the average number of edge and planar features as well as average running time of measurement processing, optimization with pure odometry, and uncertainty-aware mapping. We see that features increase along with more LiDARs, and the time for measurement preprocessing arises. The time for odometry increases because the system needs to spend more time dealing with geometric constraints. The mapping time does not grow by much since we use the voxel grid filter to bind the global map’s complexity. We also provide the running time on an Intel NUC in the supplementary material [81].

To demonstrate that more features boost the system, we conduct experiments in two cases: normal speed and high speed. We use the original RV sequence in the first case. To

TABLE VI
ATE GIVEN DIFFERENT EXTRINSICS FROM BAD TO GOOD: INJECT PERTURBATION, INITIALIZATION, AND CAD MODEL.

Case	Extrinsic Source	Rotation [deg]			Translation [m]			ATE: $\text{RMSE}_t[m]$ ($\text{RMSE}_R[deg]$)			
		x	y	z	x	y	z	M-LOAM-wo-ua	M-LOAM	A-LOAM	LEGO-LOAM
RHD (Left-Right)	Inject Perturbation	49.629	8.236	11.193	0.133	-0.440	-0.042	7.74(29.63)	0.88(8.10)	4.16(17.79)	—
	Initialization	36.300	0.069	-3.999	0.113	-0.472	-0.103	0.90(6.46)	0.79(6.92)	1.11(6.44)	—
	CAD Model	40.000	0.000	0.000	0.000	-0.456	-0.122	0.53(3.61)	0.20(2.43)	0.53(3.94)	—
RV (Top-Front)	Inject Perturbation	8.183	16.629	12.134	0.636	0.139	-1.031	0.75(4.05)	0.56(3.33)	17.85(15.46)	1.06(6.01)
	Initialization	1.320	7.264	3.011	-0.324	0.227	0.000	0.67(3.45)	0.60(3.23)	11.72(8.37)	0.90(4.06)
	CAD Model	0.000	10.000	0.000	0.795	0.000	-1.364	0.48(2.29)	0.43(2.56)	12.95(5.40)	0.73(2.44)



(a) RPE in the case of 3m/s. From one to four LiDARs, the median values of the rotation and translation error (in percentage) in odometry are: (56.53deg, 20.19%), (54.53deg, 19.29%), (48.08deg, 17.57%), (**42.96deg, 15.73%**) respectively, while those in the mapping are: (6.27deg, 2.35%), (6.26deg, 2.16%), (6.77deg, 2.32%), (**6.45deg, 2.14%**) respectively.

(b) RPE in the case of 9m/s. From one to four LiDARs, the median values of the rotation and translation error (in percentage) in odometry are: (29.38deg, 11.56%), (28.67deg, 11.00%), (24.60deg, 9.83%), (**21.02deg, 8.01%**) respectively, while those in the mapping are: (6.86deg, 2.42%), (6.43deg, 2.19%), (7.04deg, 2.24%), (**6.06deg, 2.11%**) respectively.

Fig. 22. RPE of M-LOAM on the RV sequence with different numbers of LiDARs in two cases. Better visualization in the colored version.

TABLE VII
AVERAGE FEATURE NUMBER AND RUNNING TIME ON A DESKTOP OF M-LOAM ON THE RV SEQUENCE WITH DIFFERENT LiDAR SETUPS.

Setup	One-LiDAR	Two-LiDAR	Three-LiDAR	Four-LiDAR
Edge features	1061	1366	1604	1851
Planar features	4721	5881	7378	8631
Measurement [ms]	4.6 ± 0.4	4.8 ± 0.5	5.5 ± 0.7	6.0 ± 0.7
Odometry [ms]	27 ± 5	57 ± 7	69 ± 7	73 ± 9
Mapping [ms]	78 ± 11	91 ± 13	111 ± 16	126 ± 15

simulate that the vehicle is moving faster in the second case, we extract one frame from every three frames to construct a new dataset. We evaluate the odometry and mapping of these setups in Fig. 22. The errors of the odometry decrease if more LiDARs are used. In the second case, the median values of Four-LiDAR-Odom are smaller than those of One-LiDAR-Odom around 8deg relative rotation error and 3.5% translation error. But this improvement in mapping is small because the map already provides sufficient constraints. When the vehicle is moving at a higher speed, the global map becomes sparser. Consequently, the improvement of mapping on multiple LiDARs is noticeable. The boxplot of the Four-LiDAR setup has a smaller variance than others.

F. Running Time Analysis

running time with handheld device, indoor vehicle, outdoor and different numbers of LiDARs

X. DISCUSSION

A. Main Advantages

We highlight that the proposed M-LOAM is a robust, reliable, and complete system to provide accurate calibration, odometry, and mapping results for different platforms. We can extend M-LOAM to many kinds of LiDAR combinations, as shown in experiments. A typical application of M-LOAM is autonomous driving, where the multi-LiDAR system is gradually becoming a standard setup on vehicles. As verified in the experiments, the usage of multiple LiDARs boosts the SLAM performance in both robustness and accuracy. For other perception problems such as 3D object detection and tracking [86], the multi-LiDAR systems are also beneficial.

As compared with the SOTA, M-LOAM introduces the sliding window-based tightly-coupled odometry to fuse multiple LiDARs and the uncertainty-aware mapping to maintain the globally consistent map. Furthermore, rather than operating calibrated and merged point clouds directly, it processes the multi-LiDAR measurements in a separate way. This pipeline is advantageous: 1) programs (e.g., segmentation and feature

extraction) can be easily parallelized, 2) LiDAR's scan models can be used to generate a range image without data loss, and 3) the extrinsic perturbation on the system can be formulated. We consider that the above improvements enable M-LOAM to outperform A-LOAM on most sequences. Compared with LEGO-LOAM, which uses ground features, M-LOAM is more applicable to different applications. Nevertheless, integrating M-LOAM with the ground-optimization pipeline of LEGO-LOAM for mobile robots is encouraging.

The Gaussian distribution is our core hypothesis in modeling data uncertainty. Based on it, we use a tractable method to estimate covariances of poses (derived from information matrices) and extrinsics (given a sampling covariance after calibration). Even though these covariances are approximate, as shown in experiments, e.g., Fig. 20, the proposed uncertainty-aware operation significantly improves the robustness of M-LOAM against degeneracy and extreme extrinsic perturbation.

B. Limitations

We recognize that our proposed calibration and SLAM method has limitations. First, our calibration process requires pre-set thresholds, which are obtained from experiences. Its accuracy is also not perfect for applications such as HD map construction. In practice, the error should be smaller than $0.01m$ and $1deg$. Otherwise, the calibration error is proportionally propagated to the map and deteriorates the map quality. This effect cannot be entirely eliminated even though the extrinsic perturbation is modeled by our method.

Second, our system utilizes several point cloud registrations in different phases to estimate states. As a typical non-convex problem, registration requires a good initial transformation. But LiDARs only produce a low-frequency data stream, making this problem sometimes challenging. For example, when a robot moves and turns at a high frequency, our method barely tracks its poses. Also, we use the linear model to interpolate sensors' poses, which cannot represent smooth or fast motion well. In these cases, it would be better to use high-order curves such as B-spline for interpolation [87].

Finally, we extract the simple edge and planar points from environments. However, these features present drawbacks in real tests. For instance, they only provide constraints in their perpendicular directions. In a long tunnel, where all planes are mostly parallel, M-LOAM may fail. Another example is that such features do not have enough recognition power to enable robust matching across frames with large viewpoint changes. As compared with surfel-based or visual features, they are less useful for tasks such as place recognition and relocalization.

XI. CONCLUSION AND FUTURE WORK

In this paper, we propose a complete and robust solution for multi-LiDAR extrinsic calibration and SLAM. This approach contains several desirable features, including fast segmentation for noise removal, motion and extrinsic initialization, online extrinsic calibration with convergence identification, a tightly coupled M-LO, and uncertainty-aware multi-LiDAR mapping. We conduct extensive experiments covering scenarios from

indoor offices to outdoor urban roads for evaluation. Our approach calibrates kinds of multi-LiDAR systems for different platforms. It yields accuracies centimeters in translation and deci-degrees in rotation and is comparable to a SOTA target-based method. For SLAM, the proposed system typically reaches a localization accuracy below 40cm in medium-scale ($> 150m$) scenarios and of a few meters in the large-scale urban roads ($> 3.2km$). For the benefit of the community, we make our implementation open-source.

There are several directions for future research. Adding a loop-closure module into our systems is desirable, which helps correct the accumulated drift and keep the global map [88]. Another research direction concerns object-centric SLAM. Two challenges are recently growing in the community. On the one hand, the widely used low-level geometric features are not representative and sensitive to viewpoint change. On the other hand, data sparsity and occlusion in LiDAR-based object detectors are the dominant bottlenecks. A possible solution to them is to develop a SLAM approach which can use object-level features to optimize both ego-motion and motion of dynamic objects. Trials on cameras or visual-inertial systems have been proposed in [89]–[91], while works on LiDARs are rare. Finally, extending the our approach with sensors in various modalities, e.g., IMUs [5], radars [92] and event-cameras [93] is promising. For instance, we can propagate the IMU noise model to predict pose uncertainties, or the proposed convergence criteria can be used for the extrinsic calibration of multi-model sensors.

APPENDIX

A. Jacobians of Residuals

The state vector is defined as $\mathbf{x} = [\mathbf{t}, \mathbf{q}]$. We convert \mathbf{q} into a rotation matrix \mathbf{R} by the Rodrigues formula [94]:

$$\mathbf{R} = (q_w^2 - \mathbf{q}_{xyz}^\top \mathbf{q}_{xyz})\mathbf{I} + 2\mathbf{q}_{xyz}\mathbf{q}_{xyz}^\top + 2q_w\mathbf{q}_{xyz}^\wedge, \quad (36)$$

1) *Jacobians of $\mathbf{r}_{\mathcal{H}}$* : The residuals in (9) are rewritten as:

$$\begin{aligned} \mathbf{r}_{\mathcal{H}}(\mathbf{x}, \mathbf{p}) &= [\mathbf{w}^\top (\mathbf{R}\mathbf{p} + \mathbf{t}) + d]\mathbf{w} \\ &= \text{diag}(\mathbf{w}) \begin{bmatrix} \mathbf{w}^\top \\ \mathbf{w}^\top \\ \mathbf{w}^\top \end{bmatrix} (\mathbf{R}\mathbf{p} + \mathbf{t}) + d\mathbf{w} \\ &= \mathbf{W}(\mathbf{R}\mathbf{p} + \mathbf{t}) + d\mathbf{w}. \end{aligned} \quad (37)$$

Using the left perturbation: $\mathbf{R}\exp(\delta\phi^\wedge) \approx \mathbf{R}(\mathbf{I} + \delta\phi^\wedge)$, the Jacobians of the rotation and translation are calculated as:

$$\begin{aligned} \frac{\partial \mathbf{r}_{\mathcal{H}}(\mathbf{x}, \mathbf{p})}{\partial \mathbf{x}} &= \left[\frac{\partial \mathbf{r}_{\mathcal{H}}(\mathbf{x}, \mathbf{p})}{\partial \mathbf{t}}, \frac{\partial \mathbf{r}_{\mathcal{H}}(\mathbf{x}, \mathbf{p})}{\partial \mathbf{q}} \right], \\ &= [\mathbf{W}, -\mathbf{W}\mathbf{R}\mathbf{p}^\wedge, \mathbf{0}_{3 \times 1}]. \end{aligned} \quad (38)$$

where the quaternion is updated according to $\delta \mathbf{q} \approx [\frac{1}{2}\delta\phi, 1]^\top$.

2) *Jacobians of residuals in $f_{\mathcal{M}}$ for Online Calibration*: The objective function in (21) has two terms: $f_{\mathcal{M}}(\mathcal{X}_v)$ and $f_{\mathcal{M}}(\mathcal{X}_e)$. For the first term, the Jacobians are given by

$$\frac{\partial \mathbf{r}(\mathbf{x}_p^{-1}\mathbf{x}_k, \mathbf{p})}{\partial \mathbf{x}_k} = [\mathbf{W}\mathbf{R}_p^\top, -\mathbf{W}\mathbf{R}_p^\top \mathbf{R}_k \mathbf{p}^\wedge, \mathbf{0}_{3 \times 1}], \quad (39)$$

where $k \in [p+1, N+1]$. Since the second term has the same form as (9), the Jacobians are given by (38) as:

$$\frac{\partial \mathbf{r}(\mathbf{x}_{li}^b, \mathbf{p})}{\partial \mathbf{x}_{li}^b} = [\mathbf{W}, -\mathbf{W}\mathbf{R}_{li}^b \mathbf{p}^\wedge, \mathbf{0}_{3 \times 1}], \quad (40)$$

where $i \in [2, I]$.

3) *Jacobians of residuals in $f_{\mathcal{M}}$ for Pure Odometry:* The Jacobians of the residuals in (22) are computed as:

$$\frac{\partial \mathbf{r}(\mathbf{x}_p^{-1} \mathbf{x}_k \mathbf{x}_{li}^b, \mathbf{p})}{\partial \mathbf{x}_k} = [\mathbf{W}\mathbf{R}_p^\top, -\mathbf{W}\mathbf{R}_p^\top \mathbf{R}_k (\mathbf{R}_{li}^b \mathbf{p} + \mathbf{t}_{li}^b)^\wedge, \mathbf{0}_{3 \times 1}], \quad (41)$$

where $i \in [1, I]$ and $k \in [p+1, N+1]$.

B. Marginalization

According to the sliding-window formulation, several states will be marginalized out after optimization. For the whole state vector \mathcal{X} , let us denote \mathcal{X}_m as the set of states to be marginalized, \mathcal{X}_r as the set of remaining states which are independent to \mathcal{X}_m , and \mathcal{X}_n as the irrelevant states. Due to conditional independence, the following marginalization step only involves the states containing \mathcal{X}_m and \mathcal{X}_r .

By linearizing the cost function (20) at a fixed point, we will operate on the linear problem: $\Lambda \delta \mathcal{X} = -\mathbf{g}$, where $\Lambda = \sum \mathbf{J}^\top \Sigma^{-1} \mathbf{J}$ is the *information matrix*, $\mathbf{g} = \mathbf{J}^\top \Sigma^{-1} \mathbf{r}$, \mathbf{r} is the residual, \mathbf{J} is the Jacobian matrix of the residual w.r.t current states, Σ is the covariance matrix, and $\delta \mathcal{X}$ is the state vector which minimizes the above linear problem. After estimating $\delta \mathcal{X}$, the Gauss-Newton algorithm will update the current state vector recursively such as $\mathcal{X} \boxplus \delta \mathcal{X} \rightarrow \mathcal{X}$, where \boxplus denotes the operator of the addition of two state vectors. By representing the problem using block matrices, we have

$$\begin{bmatrix} \Lambda_{mm} & \Lambda_{mr} \\ \Lambda_{rm} & \Lambda_{rr} \end{bmatrix} \begin{bmatrix} \delta \mathcal{X}_m \\ \delta \mathcal{X}_r \end{bmatrix} = - \begin{bmatrix} \mathbf{g}_m \\ \mathbf{g}_r \end{bmatrix}. \quad (42)$$

where we apply the Schur complement to yield:

$$\begin{bmatrix} \Lambda_{mm} & \Lambda_{mr} \\ \mathbf{0} & \Lambda_{rr}^* \end{bmatrix} \begin{bmatrix} \delta \mathcal{X}_m \\ \delta \mathcal{X}_r \end{bmatrix} = - \begin{bmatrix} \mathbf{g}_m \\ \mathbf{g}_r^* \end{bmatrix}, \quad (43)$$

where

$$\begin{aligned} \Lambda_{rr}^* &= \Lambda_{rr} - \Lambda_{rm} \Lambda_{mm}^{-1} \Lambda_{mr}, \\ \mathbf{g}_r^* &= \mathbf{g}_r - \Lambda_{rm} \Lambda_{mm}^{-1} \mathbf{g}_m. \end{aligned} \quad (44)$$

We define $\mathbf{g}_{r,0} = \mathbf{g}_r^*$ at the first iteration which are fixed during the marginalization. At the next iteration, the remaining states are updated with the form of $\mathcal{X}_r \boxplus \delta \mathcal{X}_r \rightarrow \mathcal{X}_r$. We thus have the new \mathbf{g}_r^* from (44) as

$$\mathbf{g}_r^* = \mathbf{g}_{r,0} - \Lambda_{rr}^* \delta \mathcal{X}_r, \quad (45)$$

We add the resulting Λ_{rr}^* and \mathbf{g}_r^* to construct the cost function, where the constraints of the marginalized states are incorporated. This helps to maintain the consistency of the states in future optimization. The error term from the marginalization is written as $\|\mathbf{r}_{pri}\|^2 = \mathbf{g}_r^{*\top} \Lambda_{rr}^{*-1} \mathbf{g}_r^*$. Since the Ceres solver [76] uses the Jacobians to update variables, when implementing the marginalization, we need to represent

information matrices with the Jacobians. We firstly factorize Λ_{rr}^* with eigenvalues and eigenvectors:

$$\Lambda_{rr}^* = \mathbf{P} \Psi \mathbf{P}^\top. \quad (46)$$

Let $\mathbf{J}^* = \sqrt{\Psi} \mathbf{P}^\top$, $\mathbf{r}^* = \sqrt{\Psi^{-1}} \mathbf{P}^\top \mathbf{g}_r^*$, we have

$$\mathbf{J}^{*\top} \mathbf{J}^* = \Lambda_{rr}^*, \quad \mathbf{J}^{*\top} \mathbf{r}^* = \mathbf{g}_r^*. \quad (47)$$

Hence, the prior residuals are equal to $\|\mathbf{r}^* + \mathbf{J}^* \Delta \mathcal{X}_r\|^2$.

REFERENCES

- [1] S. Thrun, "Probabilistic robotics," *Communications of the ACM*, vol. 45, no. 3, pp. 52–57, 2002.
- [2] C. Cadena, L. Carlone, H. Carrillo, Y. Latif, D. Scaramuzza, J. Neira, I. Reid, and J. J. Leonard, "Past, present, and future of simultaneous localization and mapping: Toward the robust-perception age," *IEEE Transactions on robotics*, vol. 32, no. 6, pp. 1309–1332, 2016.
- [3] T. D. Barfoot, *State estimation for robotics*. Cambridge University Press, 2017.
- [4] J. Jiao, Y. Yu, Q. Liao, H. Ye, R. Fan, and M. Liu, "Automatic calibration of multiple 3d lidars in urban environments," in *2019 IEEE/RSJ International Conference on Intelligent Robots and Systems (IROS)*, 2019, pp. 15–20.
- [5] H. Ye, Y. Chen, and M. Liu, "Tightly coupled 3d lidar inertial odometry and mapping," in *2019 IEEE International Conference on Robotics and Automation (ICRA)*, 2019.
- [6] R. Kesten, M. Usman, J. Houston, T. Pandya, K. Nadhamuni, A. Ferreira, M. Yuan, B. Low, A. Jain, P. Ondruska, S. Omari, S. Shah, A. Kulkarni, A. Kazakova, C. Tao, L. Platinsky, W. Jiang, and V. Shet, "Lyft level 5 av dataset 2019," [urlhttps://level5.lyft.com/dataset/](https://level5.lyft.com/dataset/), 2019.
- [7] P. Sun, H. Kretzschmar, X. Dotiwalla, A. Chouard, V. Patnaik, P. Tsui, J. Guo, Y. Zhou, Y. Chai, B. Caine, et al., "Scalability in perception for autonomous driving: Waymo open dataset," in *Proceedings of the IEEE/CVF Conference on Computer Vision and Pattern Recognition*, 2020, pp. 2446–2454.
- [8] S. Agarwal, A. Vora, G. Pandey, W. Williams, H. Kourous, and J. McBride, "Ford multi-av seasonal dataset," *arXiv preprint arXiv:2003.07969*, 2020.
- [9] D. Barnes, M. Gadd, P. Murcutt, P. Newman, and I. Posner, "The oxford radar robotcar dataset: A radar extension to the oxford robotcar dataset," *arXiv preprint arXiv:1909.01300*, 2019.
- [10] J. Geyer, Y. Kassahun, M. Mahmudi, X. Ricou, R. Durgesh, A. S. Chung, L. Hauswald, V. H. Pham, M. Mühlegg, S. Dorn, et al., "A2d2: Audi autonomous driving dataset," *arXiv preprint arXiv:2004.06320*, 2020.
- [11] T. Liu, Q. Liao, L. Gan, F. Ma, J. Cheng, X. Xie, Z. Wang, Y. Chen, Y. Zhu, S. Zhang, et al., "Hercules: An autonomous logistic vehicle for contact-less goods transportation during the covid-19 outbreak," *arXiv preprint arXiv:2004.07480*, 2020.
- [12] J. Jiao, Q. Liao, Y. Zhu, T. Liu, Y. Yu, R. Fan, L. Wang, and M. Liu, "A novel dual-lidar calibration algorithm using planar surfaces," in *IEEE Intelligent Vehicles Symposium (IV)*, 2019.
- [13] M. Li, H. Yu, X. Zheng, and A. I. Mourikis, "High-fidelity sensor modeling and self-calibration in vision-aided inertial navigation," in *Robotics and Automation (ICRA)*, 2014 IEEE International Conference on, IEEE, 2014, pp. 409–416.
- [14] Z. Yang and S. Shen, "Monocular visual-inertial fusion with online initialization and camera-imu calibration," in *2015 IEEE International Symposium on Safety, Security, and Rescue Robotics (SSRR)*. IEEE, 2015, pp. 1–8.
- [15] T. Qin, P. Li, and S. Shen, "Vins-mono: A robust and versatile monocular visual-inertial state estimator," *IEEE Transactions on Robotics*, vol. 34, no. 4, pp. 1004–1020, 2018.
- [16] J. Zhang and S. Singh, "Loam: Lidar odometry and mapping in real-time," in *Robotics: Science and Systems*, vol. 2, 2014, p. 9.
- [17] T. Shan and B. Englot, "Lego-loam: Lightweight and ground-optimized lidar odometry and mapping on variable terrain," in *2018 IEEE/RSJ International Conference on Intelligent Robots and Systems (IROS)*. IEEE, 2018, pp. 4758–4765.
- [18] J. Lin and F. Zhang, "Loam_livox: A fast, robust, high-precision lidar odometry and mapping package for lidars of small fov," *arXiv preprint arXiv:1909.06700*, 2019.
- [19] T. D. Barfoot and P. T. Furgale, "Associating uncertainty with three-dimensional poses for use in estimation problems," *IEEE Transactions on Robotics*, vol. 30, no. 3, pp. 679–693, 2014.

- [20] F. Pomerleau, F. Colas, R. Siegwart, and S. Magnenat, "Comparing icp variants on real-world data sets," *Autonomous Robots*, vol. 34, no. 3, pp. 133–148, 2013.
- [21] A. Segal, D. Haehnel, and S. Thrun, "Generalized-icp," in *Robotics: science and systems*, vol. 2, no. 4, 2009, p. 435.
- [22] J. Serafin and G. Grisetti, "Ntcp: Dense normal based point cloud registration," in *Intelligent Robots and Systems (IROS)*, 2015 IEEE/RSJ International Conference on. IEEE, 2015, pp. 742–749.
- [23] M. Magnusson, A. Lilienthal, and T. Duckett, "Scan registration for autonomous mining vehicles using 3d-ndt," *Journal of Field Robotics*, vol. 24, no. 10, pp. 803–827, 2007.
- [24] J. Behley and C. Stachniss, "Efficient surfel-based slam using 3d laser range data in urban environments," in *Robotics: Science and Systems*, 2018.
- [25] X. Chen, A. Milioto, E. Palazzolo, P. Giguère, J. Behley, and C. Stachniss, "Suma++: Efficient lidar-based semantic slam," in *2019 IEEE/RSJ International Conference on Intelligent Robots and Systems (IROS)*. IEEE, 2019, pp. 4530–4537.
- [26] W. S. Grant, R. C. Voorhies, and L. Itti, "Finding planes in lidar point clouds for real-time registration," in *2013 IEEE/RSJ International Conference on Intelligent Robots and Systems*. IEEE, 2013, pp. 4347–4354.
- [27] M. Velas, M. Spanel, and A. Herout, "Collar line segments for fast odometry estimation from velodyne point clouds," in *2016 IEEE International Conference on Robotics and Automation (ICRA)*. IEEE, 2016, pp. 4486–4495.
- [28] G. Pandey, S. Giri, and J. R. McBride, "Alignment of 3d point clouds with a dominant ground plane," in *Intelligent Robots and Systems (IROS)*, 2017 IEEE/RSJ International Conference on. IEEE, 2017, pp. 2143–2150.
- [29] S. W. Chen, G. V. Nardari, E. S. Lee, C. Qu, X. Liu, R. A. F. Romero, and V. Kumar, "Sloam: Semantic lidar odometry and mapping for forest inventory," *IEEE Robotics and Automation Letters*, vol. 5, no. 2, pp. 612–619, 2020.
- [30] K. Ji, H. Chen, H. Di, J. Gong, G. Xiong, J. Qi, and T. Yi, "Cpfg-slam: a robust simultaneous localization and mapping based on lidar in off-road environment," in *2018 IEEE Intelligent Vehicles Symposium (IV)*. IEEE, 2018, pp. 650–655.
- [31] M. Bosse, R. Zlot, and P. Flick, "Zebedee: Design of a spring-mounted 3-d range sensor with application to mobile mapping," *IEEE Transactions on Robotics*, vol. 28, no. 5, pp. 1104–1119, 2012.
- [32] A. Pfrunder, P. V. Borges, A. R. Romero, G. Catt, and A. Elfes, "Real-time autonomous ground vehicle navigation in heterogeneous environments using a 3d lidar," in *2017 IEEE/RSJ International Conference on Intelligent Robots and Systems (IROS)*. IEEE, 2017, pp. 2601–2608.
- [33] J. Zhang, M. Kaess, and S. Singh, "On degeneracy of optimization-based state estimation problems," in *2016 IEEE International Conference on Robotics and Automation (ICRA)*. IEEE, 2016, pp. 809–816.
- [34] A. Hinduja, B.-J. Ho, and M. Kaess, "Degeneracy-aware factors with applications to underwater slam," in *2019 IEEE/RSJ International Conference on Intelligent Robots and Systems (IROS)*, 2019, pp. 1293–1299.
- [35] J. Zhang and S. Singh, "Enabling aggressive motion estimation at low-drift and accurate mapping in real-time," in *2017 IEEE International Conference on Robotics and Automation (ICRA)*. IEEE, 2017, pp. 5051–5058.
- [36] W. Zhen and S. Scherer, "Estimating the localizability in tunnel-like environments using lidar and uwb," in *2019 International Conference on Robotics and Automation (ICRA)*. IEEE, 2019, pp. 4903–4908.
- [37] Z. Rong and N. Michael, "Detection and prediction of near-term state estimation degradation via online nonlinear observability analysis," in *2016 IEEE International Symposium on Safety, Security, and Rescue Robotics (SSRR)*. IEEE, 2016, pp. 28–33.
- [38] S. Lynen, M. W. Achtelik, S. Weiss, M. Chli, and R. Siegwart, "A robust and modular multi-sensor fusion approach applied to mav navigation," in *2013 IEEE/RSJ international conference on intelligent robots and systems*. IEEE, 2013, pp. 3923–3929.
- [39] G. Wan, X. Yang, R. Cai, H. Li, Y. Zhou, H. Wang, and S. Song, "Robust and precise vehicle localization based on multi-sensor fusion in diverse city scenes," in *2018 IEEE International Conference on Robotics and Automation (ICRA)*. IEEE, 2018, pp. 4670–4677.
- [40] S. Zhao, Z. Fang, H. Li, and S. Scherer, "A robust laser-inertial odometry and mapping method for large-scale highway environments," in *2019 IEEE/RSJ International Conference on Intelligent Robots and Systems (IROS)*. IEEE, 2019.
- [41] X. Zuo, P. Geneva, Y. Yang, W. Lee, Y. Liu, and G. Huang, "Lic-fusion: Lidar-inertial-camera odometry," in *2013 IEEE/RSJ international conference on intelligent robots and systems*. IEEE, 2013.
- [42] C. Qin, H. Ye, C. E. Pranata, J. Han, and M. Liu, "Lins: A lidar-inertial state estimator for robust and fast navigation," *arXiv preprint arXiv:1907.02233*, 2019.
- [43] G. Hemann, S. Singh, and M. Kaess, "Long-range gps-denied aerial inertial navigation with lidar localization," in *2016 IEEE/RSJ International Conference on Intelligent Robots and Systems (IROS)*. IEEE, 2016, pp. 1659–1666.
- [44] T. Lowe, S. Kim, and M. Cox, "Complementary perception for handheld slam," *IEEE Robotics and Automation Letters*, vol. 3, no. 2, pp. 1104–1111, 2018.
- [45] C. Le Gentil, T. Vidal-Calleja, and S. Huang, "In2lama: Inertial lidar localization and mapping," in *2019 International Conference on Robotics and Automation (ICRA)*. IEEE, 2019, pp. 6388–6394.
- [46] C. L. Gentil, T. Vidal-Calleja, and S. Huang, "In2laama: Inertial lidar localisation autocalibration and mapping," *arXiv preprint arXiv:1905.09517*, 2019.
- [47] J. Graeter, A. Wilczynski, and M. Lauer, "Limo: Lidar-monocular visual odometry," in *2018 IEEE/RSJ International Conference on Intelligent Robots and Systems (IROS)*. IEEE, 2018, pp. 7872–7879.
- [48] S.-S. Huang, Z.-Y. Ma, T.-J. Mu, H. Fu, and S.-M. Hu, "Lidar-monocular visual odometry using point and line features," 2020.
- [49] X. Zuo, P. Geneva, Y. Yang, W. Ye, Y. Liu, and G. Huang, "Visual-inertial localization with prior lidar map constraints," *IEEE Robotics and Automation Letters*, vol. 4, no. 4, pp. 3394–3401, 2019.
- [50] H. Ye, H. Huang, and M. Liu, "Monocular direct sparse localization in a prior 3d surfel map," in *2020 International Conference on Robotics and Automation (ICRA)*. IEEE, 2020.
- [51] H. Huang, H. Ye, Y. Sun, and M. Liu, "Gmmloc: Structure consistent visual localization with gaussian mixture models," *IEEE Robotics and Automation Letters*, vol. 5, no. 4, pp. 5043–5050, 2020.
- [52] C. Gao and J. R. Spletzer, "On-line calibration of multiple lidars on a mobile vehicle platform," in *Robotics and Automation (ICRA)*, 2010 IEEE International Conference on. IEEE, 2010, pp. 279–284.
- [53] M. He, H. Zhao, F. Davoine, J. Cui, and H. Zha, "Pairwise lidar calibration using multi-type 3d geometric features in natural scene," in *Intelligent Robots and Systems (IROS)*, 2013 IEEE/RSJ International Conference on. IEEE, 2013, pp. 1828–1835.
- [54] B. Xue, J. Jiao, Y. Zhu, L. Zhen, D. Han, M. Liu, and R. Fan, "Automatic calibration of dual-lidars using two poles stickered with retro-reflective tape," in *2019 IEEE International Conference on Imaging Systems and Techniques (IST)*. IEEE, 2019, pp. 1–6.
- [55] R. Kümmerle, G. Grisetti, and W. Burgard, "Simultaneous calibration, localization, and mapping," in *2011 IEEE/RSJ International Conference on Intelligent Robots and Systems*. IEEE, 2011, pp. 3716–3721.
- [56] A. Teichman, S. Miller, and S. Thrun, "Unsupervised intrinsic calibration of depth sensors via slam," in *Robotics: Science and Systems*, vol. 248, 2013, p. 3.
- [57] L. Heng, G. H. Lee, and M. Pollefeys, "Self-calibration and visual slam with a multi-camera system on a micro aerial vehicle," *Autonomous robots*, vol. 39, no. 3, pp. 259–277, 2015.
- [58] Z. Ouyang, L. Hu, Y. LU, Z. W. Wang, X. Peng, and L. Kneip, "Online calibration of exterior orientations of a vehicle-mounted surround-view camera system," in *2020 IEEE International Conference on Robotics and Automation (ICRA)*. IEEE, 2020.
- [59] Z. Yang, T. Liu, and S. Shen, "Self-calibrating multi-camera visual-inertial fusion for autonomous mavs," in *2016 IEEE/RSJ International Conference on Intelligent Robots and Systems (IROS)*. IEEE, 2016, pp. 4984–4991.
- [60] T. Qin and S. Shen, "Online temporal calibration for monocular visual-inertial systems," in *2018 IEEE/RSJ International Conference on Intelligent Robots and Systems (IROS)*. IEEE, 2018, pp. 3662–3669.
- [61] C. Le Gentil, T. Vidal-Calleja, and S. Huang, "3d lidar-imu calibration based on upsampled preintegrated measurements for motion distortion correction," in *2018 IEEE International Conference on Robotics and Automation (ICRA)*. IEEE, 2018, pp. 2149–2155.
- [62] V. Ila, L. Polok, M. Solony, P. Smrz, and P. Zemcik, "Fast covariance recovery in incremental nonlinear least-squares solvers," in *2015 IEEE International Conference on Robotics and Automation (ICRA)*. IEEE, 2015, pp. 4636–4643.
- [63] F. Pomerleau, A. Breitenmoser, M. Liu, F. Colas, and R. Siegwart, "Noise characterization of depth sensors for surface inspections," in *2012 2nd International Conference on Applied Robotics for the Power Industry (CARPI)*. IEEE, 2012, pp. 16–21.

- [64] M. Bosse, G. Agamennoni, I. Gilitschenski, et al., Robust estimation and applications in robotics. Now Publishers, 2016.
- [65] T.-C. Dong-Si and A. I. Mourikis, “Motion tracking with fixed-lag smoothing: Algorithm and consistency analysis,” in 2011 IEEE International Conference on Robotics and Automation. IEEE, 2011, pp. 5655–5662.
- [66] I. Bogoslavskyi and C. Stachniss, “Fast range image-based segmentation of sparse 3d laser scans for online operation,” in 2016 IEEE/RSJ International Conference on Intelligent Robots and Systems (IROS). IEEE, 2016, pp. 163–169.
- [67] Z. Taylor and J. Nieto, “Motion-based calibration of multimodal sensor extrinsics and timing offset estimation,” IEEE Transactions on Robotics, vol. 32, no. 5, pp. 1215–1229, 2016.
- [68] S. Leutenegger, P. Furgale, V. Rabaud, M. Chli, K. Konolige, and R. Siegwart, “Keyframe-based visual-inertial slam using nonlinear optimization,” Proceedings of Robotics Science and Systems (RSS) 2013, 2013.
- [69] R. B. Rusu and S. Cousins, “3d is here: Point cloud library (pcl),” in 2011 IEEE international conference on robotics and automation. IEEE, 2011, pp. 1–4.
- [70] A. Censi, “An accurate closed-form estimate of icp’s covariance,” in Proceedings 2007 IEEE international conference on robotics and automation. IEEE, 2007, pp. 3167–3172.
- [71] S. Bonnabel, M. Barczyk, and F. Goulette, “On the covariance of icp-based scan-matching techniques,” in 2016 American Control Conference (ACC). IEEE, 2016, pp. 5498–5503.
- [72] M. Brossard, S. Bonnabel, and A. Barrau, “A new approach to 3d icp covariance estimation,” IEEE Robotics and Automation Letters, vol. 5, no. 2, pp. 744–751, 2020.
- [73] D. Landry, F. Pomerleau, and P. Giguere, “Cello-3d: Estimating the covariance of icp in the real world,” in 2019 International Conference on Robotics and Automation (ICRA). IEEE, 2019, pp. 8190–8196.
- [74] W. Maddern, G. Pascoe, C. Linegar, and P. Newman, “1 year, 1000 km: The oxford robotcar dataset,” The International Journal of Robotics Research, vol. 36, no. 1, pp. 3–15, 2017.
- [75] Y. Kim and A. Kim, “On the uncertainty propagation: Why uncertainty on lie groups preserves monotonicity?” in 2017 IROS. IEEE, 2017, pp. 3425–3432.
- [76] S. Agarwal, K. Mierle, and Others, “Ceres solver,” <http://ceres-solver.org>.
- [77] N. Koenig and A. Howard, “Design and use paradigms for gazebo, an open-source multi-robot simulator,” in 2004 IEEE/RSJ International Conference on Intelligent Robots and Systems (IROS)(IEEE Cat. No. 04CH37566), vol. 3. IEEE, 2004, pp. 2149–2154.
- [78] S. Mou, Y. Chang, W. Wang, and D. Zhao, “An optimal lidar configuration approach for self-driving cars,” arXiv preprint arXiv:1805.07843, 2018.
- [79] L. Zheng, Y. Zhu, B. Xue, M. Liu, and R. Fan, “Low-cost gps-aided lidar state estimation and map building,” in 2019 IEEE International Conference on Imaging Systems and Techniques (IST). IEEE, 2019, pp. 1–6.
- [80] Y. Zhu, B. Xue, L. Zheng, H. Huang, M. Liu, and R. Fan, “Real-time, environmentally-robust 3d lidar localization,” in 2019 IEEE International Conference on Imaging Systems and Techniques (IST). IEEE, 2019, pp. 1–6.
- [81] J. Jiao, H. Ye, Y. Zhu, and M. Liu, “Supplementary material to: Robust odometry and mapping for multi-lidar systems with online extrinsic calibration,” Tech. Rep. [Online]. Available: <https://ram-lab.com/file/site/m-loam/supp.pdf>
- [82] D. Droschel, J. Stückler, and S. Behnke, “Local multi-resolution representation for 6d motion estimation and mapping with a continuously rotating 3d laser scanner,” in 2014 IEEE International Conference on Robotics and Automation (ICRA). IEEE, 2014, pp. 5221–5226.
- [83] J. Razlaw, D. Droschel, D. Holz, and S. Behnke, “Evaluation of registration methods for sparse 3d laser scans,” in 2015 European Conference on Mobile Robots (ECMR). IEEE, 2015, pp. 1–7.
- [84] K. Huang and C. Stachniss, “On geometric models and their accuracy for extrinsic sensor calibration,” in 2018 IEEE International Conference on Robotics and Automation (ICRA). IEEE, 2018, pp. 1–9.
- [85] Z. Zhang and D. Scaramuzza, “A tutorial on quantitative trajectory evaluation for visual (-inertial) odometry,” in 2018 IEEE/RSJ International Conference on Intelligent Robots and Systems (IROS). IEEE, 2018, pp. 7244–7251.
- [86] J. Jianhao, Y. Peng, T. Lei, and L. Ming, “Mlod: Awareness of extrinsic perturbation in multi-lidar 3d object detection for autonomous driving,” in 2020 IEEE/RSJ International Conference on Intelligent Robots and Systems (IROS), 2020.
- [87] C. Park, P. Moghadam, J. Williams, S. Kim, S. Sridharan, and C. Fookes, “Elasticity meets continuous-time: Map-centric dense 3d lidar slam,” arXiv preprint arXiv:2008.02274, 2020.
- [88] X. Chen, T. Labe, A. Milioto, T. Röhling, O. Vysotska, A. Haag, J. Behley, C. Stachniss, and F. Fraunhofer, “Overlapnet: Loop closing for lidar-based slam,” in Proc. of Robotics: Science and Systems (RSS), 2020.
- [89] S. Yang and S. Scherer, “Cubeslam: Monocular 3-d object slam,” IEEE Transactions on Robotics, vol. 35, no. 4, pp. 925–938, 2019.
- [90] J. Zhang, M. Henein, R. Mahony, and V. Ila, “Vdo-slam: A visual dynamic object-aware slam system,” arXiv preprint arXiv:2005.11052, 2020.
- [91] T. Qin, T. Chen, Y. Chen, and Q. Su, “Ayp-slam: Semantic visual mapping and localization for autonomous vehicles in the parking lot,” arXiv preprint arXiv:2007.01813, 2020.
- [92] D. Barnes, M. Gadd, P. Murcutt, P. Newman, and I. Posner, “The oxford radar robotcar dataset: A radar extension to the oxford robotcar dataset,” in Proceedings of the IEEE International Conference on Robotics and Automation (ICRA), Paris, 2020. [Online]. Available: <https://arxiv.org/abs/1909.01300>
- [93] G. Gallego, T. Delbruck, G. Orchard, C. Bartolozzi, B. Taba, A. Censi, S. Leutenegger, A. Davison, J. Conradt, K. Daniilidis, et al., “Event-based vision: A survey,” arXiv preprint arXiv:1904.08405, 2019.
- [94] J. Sola, “Quaternion kinematics for the error-state kalman filter,” arXiv preprint arXiv:1711.02508, 2017.